The Hong Kong Polytechnic University

Department of Applied Physics

Oxide-based Giant Magnetoresistive Heterostructures

CHENG Wang Fai

A thesis submitted in partial fulfillment of the requirements for the Degree of Master of Philosophy

August 2007

Certificate of Originality

I hereby declare that this thesis is my own work and that, to the best of my knowledge and belief, it reproduces no material previously published or written nor material which has been accepted for the award of any other degree or diploma, except where due acknowledgement has been made in the text.

_____(Signature)

Cheng Wang Fai (Name of student)

Abstract

The giant magnetoresistance (GMR) effect was discovered in 1988 in metal multilayer structures. The effect showed a large magnetoresistance (MR) ratio up to 80% at room temperature in Fe/Cr multilayers. Since then a number of alternative structures were developed, but they invariably relied on the changes of relative magnetization directions in the magnetic layers or components to achieve high and low resistive states. The discovery of GMR effect had a strong impact on the development of computer memory technology. At present, GMR read heads are used extensively in hard disk read heads.

In my research project, oxide-based spin valve structures were deposited and characterized. $La_{0.7}Sr_{0.3}MnO_3$ (LSMO) thin films were fabricated by pulsed laser deposition. The project consists of two parts. In the first part, the effects of post annealing on LSMO films, under different oxygen pressures, were examined. During multilayer fabrication processes, different growth conditions may be necessary for various layers. Different annealing procedures, sometimes *ex situ*, have to be performed. Therefore, the stability of the layers has to be studied, in order to obtain multilayers

with desirable properties. This part of study provided useful information for investigations on epitaxial oxide multilayers.

LSMO thin films were deposited by pulsed laser deposition on (100) $LaAlO_3$ (LAO) substrates at 650 °C, with the film thicknesses varying from 20 to 50 nm. The oxygen pressures used to fabricate the films were 150 (or 100) mTorr. *In situ* annealing processes were then performed at 100 (150) mTorr. Curie temperatures (*Tc*) of the films were estimated from the peaks of the resistance-temperature (RT) graphs. For LSMO films deposited at 150 mTorr and annealed at 100 mTorr, *Tc* of the samples dropped with an increasing annealing time until about 30 minutes, beyond which the T_C started to increase. For LSMO films deposited at 100 mTorr and annealed at 150 mTorr, no signs of metal-insulation transition were observed even after 30 minutes of annealing. *Ex situ* annealing processes were also performed, testing the stability of LSMO films under post-deposition heat treatment processes after exposure to ambient conditions. The *Tc* of films were found to be strongly dependent on the annealing procedures.

In the second part of the project, pseudo spin valves were fabricated by using LSMO and $Co_{33}Fe_{67}$ (CoFe) as ferromagnetic layers. These layers had very different coercivities, an important criterion for observing GMR effect. In order to reduce

magnetic coupling between the two ferromagnetic layers, a non-magnetic and conducting spacer layer is usually required. Recent research has however shown that pseudo spin valves could be fabricated without using spacer layers. These spacerless pseudo spin valves, formed by direct deposition of polycrystalline metallic layers on epitaxial oxides, greatly reduced the difficulty in the fabrication process.

In this part of the project, the magnetotransport property of deposited LSMO\CoFe structure was investigated. Magnetoresistances of samples were measured in current-perpendicular-to-plane mode. For single-layer LSMO samples grown on (100) LAO, a negative magentoresistance behaviour was obtained. After depositing the CoFe, the magnetoresistance behaviour was changed from negative to positive. One of possible reasons for the observation is the interfacial layer formed between the metal and oxide layers, which can be treated as a non-magnetic spacer. The thickness of the interface layer was sufficiently large to decouple the two ferromagnetic layers. Relative magnetization directions of the two ferromagnetic layers can be switched independently by an external magnetic field, according to their corresponding coercivities.

Acknowledgements

I would like to acknowledge Dr. C. W. Leung, my chief supervisor, for his guidance and for patiently proofreading this thesis at various stages. I also wish to thank Dr. J. Y. Dai, my co-supervisor, Dr. K. H. Wong and Dr. C. L. Mak for providing valuable comments. Special thanks go to Miss. C. Y. Lam, Mr. M. H. Wong and Mr. W. L. Sin for training me on using the PLD system, XRD, LabView Programming and VSM. I also thank Mr. Y. K. Chan for his help and discussions on my research work. I would like to thank my research companions, Mr. H. Y. Kwong, Mr. C. H. Lau and Mr. W. C. Liu for their useful suggestions.

This work is supported by a grant from the Research Grants Council of the Hong Kong Special Administrative Region, China (Project No. PolyU 5216/06E), and a studentship from the Hong Kong Polytechnic University.

TABLE OF CONTENTS

CHAPTER 1

Introduction

Since late 1980s, numerous studies have been made on investigating the origin of the giant magnetoresistive (GMR) effect and potential enhancement of the magnetoresistive responses. Commercial devices based on GMR effect, such as read heads, magnetic field sensors and magnetic memory chips, have become available in the market. These significant progresses are due to advancements in thin film deposition techniques, making it possible to fabricate ultrathin layers of various materials with precise thicknesses.

So far, GMR investigations have been dominated by metallic structures. Metallic magnetic materials generally have spin polarization values less than 50% [1]. As the GMR ratio strongly depends on the spin polarization of the materials, perovskite manganites are good alternative materials due to their fully spin-polarized conduction bands. In addition, oxides are more tolerant towards extreme working conditions, making them more attractive for specialized operations.

This thesis is divided into six chapters. Brief reviews on the topics of magnetoresistance and half-metallic manganites are given in Chapter 2. Experimental

techniques used in the project are discussed in details in Chapter 3. These include heteroepitaxial thin film growth by pulsed laser deposition (PLD), as well as electric and magnetic characterization techniques. In Chapter 4, I will discuss the fabrication and characterization of LSMO thin films by PLD; in particular, the post annealing effect on the properties of LSMO was studied and the results will be presented. In Chapter 5, details on the fabrication and characterization of LNO\LSMO\$Co_{33}Fe_{67}$ trilayers will be presented. Finally, Chapter 6 summarizes the main results and conclusions arising from this work.

CHAPTER 2

Background Review

2.1 Magnetoresistance

2.1.1 Introduction

Magnetoresistance (MR) refers to the change of a material's resistivity under the influence of an external magnetic field. It has a variety of physical origins, depending on the material's intrinsic and extrinsic properties. MR effect is gaining importance in technological applications. It is heavily used in magnetic memories, read heads and magnetic field sensors [2]. In the following, various MR effects will be introduced. They include ordinary MR, anisotropic MR, tunneling MR, colossal MR, and giant MR. Generally, the MR ratio is defined as

$$MR(H) = \frac{\rho(H = 0) - \rho(H)}{\rho(H = 0)} \qquad (2.1.1)$$

unless otherwise stated.

2.1.2 Ordinary magnetoresistance (OMR)

For many materials, including non-magnetic metals or semiconductors, when an external magnetic flux B is applied perpendicular to the electric field, the measured resistance of the sample can be changed. It is due to the Lorentz force acting on the charge carriers:

$$F = -ev \times B \qquad (2.1.2).$$

The force has an effect on the paths of conduction electrons in the materials as shown in Fig 2.1.1. The sign of MR is usually positive, meaning there is an increased resistance with a rise of magnitude in B. However, such an MR effect is very small at moderate magnetic fields. Typically, OMR in normal metals required a magnetic field up to 1 Tesla in order to obtain a resistance change of 1%.

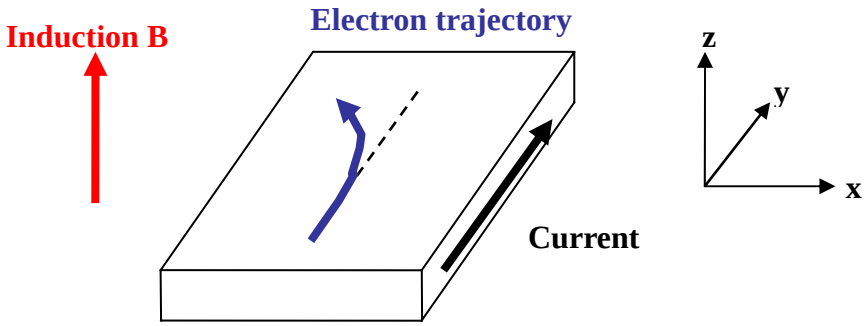

Fig. 2.1.1 Trajectory of charge carriers in a conductor under the influence of an external magnetic flux. The black arrow represents the direction of applied electric field. The blue arrow represents the electron trajectory under the influence of an applied magnetic flux B.

2.1.3 Anisotropic magnetoresistance (AMR)

When a magnetic field is applied to ferromagnetic metals or alloys, there is an additional change of resistance related to the relative orientation between magnetization and electric current. By applying a magnetic field, the direction of magnetization can be changed. Typically, the longitudinal resistance $\rho_{//}$ reaches a maximum if the current is parallel to the magnetization, and the transverse resistance $\rho_{\perp}$ reaches a minimum if the current perpendicular to the magnetization [3]. The magnitude of AMR is typically a few percent. The AMR ratio is defined as

$$AMR = \frac{\rho_{//} - \rho_{\perp}}{\rho_{//}} \qquad (2.1.3)$$

Figure 2.1.2 shows a schematic for the AMR effect. The resistivity of a film is given by

$$\rho(\theta) = \rho_{\perp} + (\rho_{//} - \rho_{\perp})\cos^2\theta \qquad (2.1.4)$$

where θ is the relative orientation between magnetization and current flow directions.

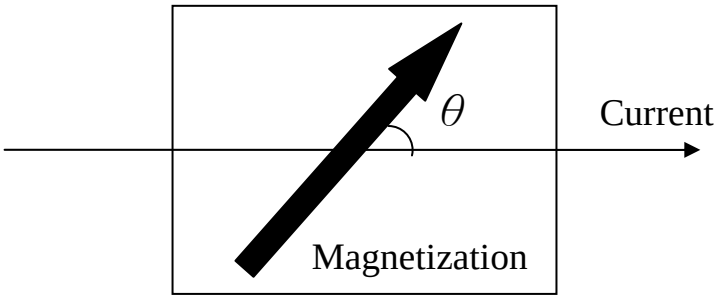

Fig. 2.1.2 Schematic diagram of AMR effect.

The physical origin of AMR effect is spin-orbit coupling [3]. When the magnetization of a material rotates, the electron cloud surrounding the nucleus is deformed, and the probability for conduction electrons to be scattered is changed (Fig.2.1.3).

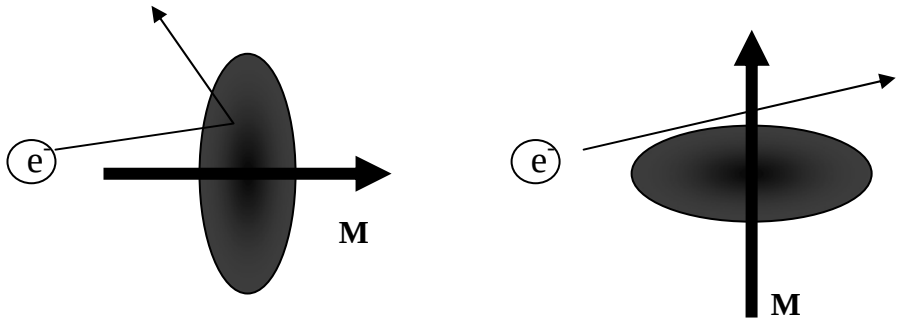

Fig. 2.1.3 Mechanism of AMR effect. Shaded regions represent the scattering cross-sections of the bounded electronic orbits. The relative orientation between current and magnetization affects the scattering of electron, giving rise to different resistance values.

The effect was previously used in magnetic read heads applications [3], with NiFe (permalloy) being commonly used due to its moderate MR (~5%) at low magnetic fields and at room temperature.

2.1.4 Tunneling magnetoresistance (TMR)

Electron tunneling effect is a quantum mechanical phenomenon. When a potential difference is applied to two electrodes across a thin insulating barrier, electrons have a finite chance to pass (tunnel) from one electrode to another. If the two electrodes are ferromagnetic, the tunneling probability for a particular spin channel would depend on the relative magnetization directions of the two ferromagnetic layers as shown in Fig 2.1.4.

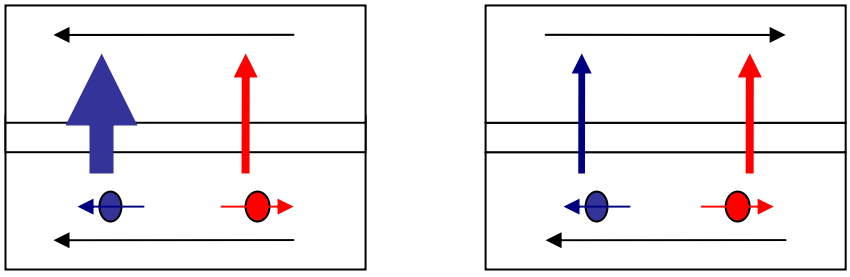

parallel antiparallel

Fig. 2.1.4 Schematic of high and low resistance states of TMR junction.

The dissimilar tunneling conductances arise from the asymmetry of spin sub-bands, which is the origin of the TMR effect. TMR ratio is defined as

$$TMR = \frac{R_{AP} - R_p}{R_p} \qquad (2.1.5)$$

where R_{ap} and R_p are resistances with the ferromagnetic layers in anti-parallel and parallel configurations, respectively.

TMR was first observed in Fe\Ge\Co junctions in 1975 [4], but the effect was not reproduced until 1995, when a TMR ratio of ~12% at room temperature was reported in CoFe\Al_2O_3\Co junctions [5]. Nowadays, TMR performances of tunnel junctions have been greatly improved, and a large MR ratio of ~230% has been reached at room temperature in CoFeB\MgO\CoFeB system [6].

2.1.5 Colossal magnetoresistance (CMR)

In mixed-valence manganites with perovskite structures, a large MR effect was discovered when the material was exposed to a high magnetic field (127000% at 77K, under a 6 Tesla field for $La_{0.67}Ca_{0.33}MnO_3$ thin films) [7]. Similarly large MR effect was also observed in complex oxides such as double perovskites and layered perovskites [8]. Because of the very large MR effect, and to distinguish it from the GMR effect, it is

called CMR. The origin of the CMR effect will be further discussed in Section 2.2.

2.1.6 Giant magnetoresistance

2.1.6.1 Introduction

The GMR effect was discovered in 1988 in Fe/Cr metallic multilayers [9]. A large MR ratio up to 80%, with H_s ~ 20 kOe, at 4.2K, was reported. The effect originated from changes in the relative magnetization orientations of magnetic layers. The GMR ratio is defined basically in the same way as TMR:

$$GMR = \frac{R_{\uparrow\downarrow} - R_{\uparrow\uparrow}}{R_{\uparrow\uparrow}} \qquad (2.1.4)$$

where $R_{\uparrow\uparrow}$ and $R_{\uparrow\downarrow}$ are the resistances of the sample, when the magnetization of the layers are in parallel and anti-parallel configurations, respectively.

The resistance of GMR structure depends on the magnetization directions of magnetic layers. In multilayered structures, magnetic layers are separated by very thin non-magnetic layers (spacer layers), in the order of Å. If a magnetic field is applied on the sample, the magnetization of layers can be switched independently. For simplicity, suppose the magnetization of layers can be oriented in only two extreme configurations (parallel and anti-parallel magnetization alignments) as shown in Fig. 2.1.5. Such a

difference in the relative alignment of magnetization vectors leads to corresponding resistance changes of the samples. Some examples of GMR multilayered structures are Fe\Cr and Co\Cu structures [9-11].

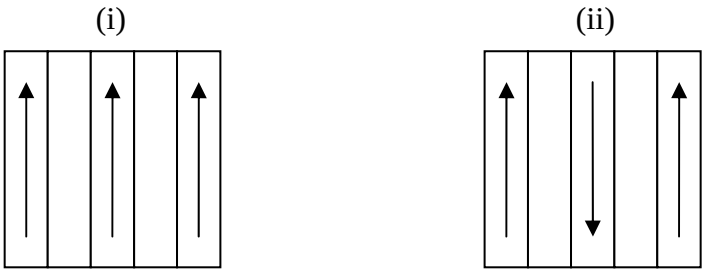

Fig. 2.1.5 Ferromagnetic (i) and antiferromagnetic (ii) configurations of magnetic/non-magnetic multilayered structures.

The discovery of GMR effect makes a strong impact on the development of computer memory technology. Previously, AMR effect was used in the fabrication of hard disk read heads. It was difficult to scale down AMR sensors in order to meet requirements of high density memories, as device resistance increases with shrinking device sizes and the MR signals would be shadowed by background noises [12]. At present, GMR read heads are used in hard disk read heads in order to achieve high density memory, due to the high MR ratio [2].

2.1.6.2 Measurement geometry

There are two measurement geometries of the GMR effect, as shown schematically in Fig 2.1.6. The first one (Fig 2.1.6(i)) is the current-perpendicular-to-the-plane (CPP) geometry, and the other one (Fig 2.1.6(ii)) is the current-in-the-plane (CIP) geometry. The fundamental physical mechanisms of the GMR effect are identical in both geometries, as explained below.

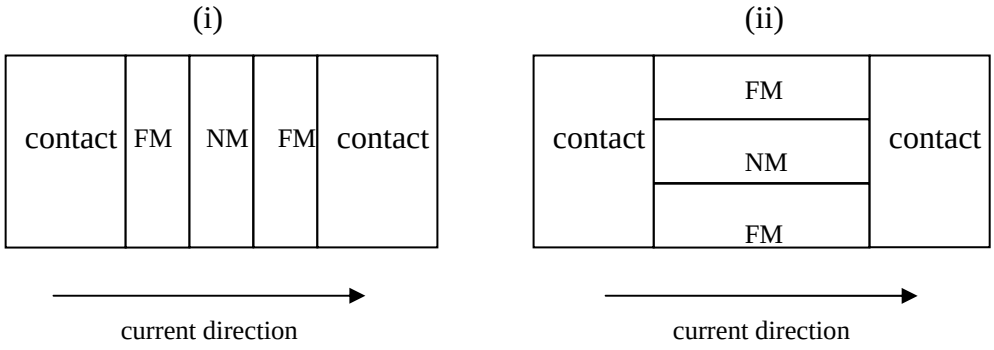

Fig. 2.1.6 Measurement geometries of MR effect. (i) current perpendicular to plane, and (ii) current in plane geometries.

CPP GMR is very attractive due to higher MR ratios compared with CIP GMR of the same structure [13, 14]. In addition, CPP MR measurements are advantageous for fundamental studies of GMR mechanism. As the current flow along normal direction to the film plane is constant in the CPP geometry, a simple series resistor model can be use

for analysis. In CIP geometry, on the other hand, the current density depends heavily on the resistance of individual layers, as well as electrode and sample geometries. CIP MR data are thus more difficult for quantitative analysis.

2.1.6.3 Origin of GMR

GMR effect can be understood by a two-current model proposed by Mott [15]. He suggested that electrical conductivity in metals can be separated into two conduction channels, corresponding to up-spin (majority spin) and down-spin (minority spin) electrons. When the temperature is sufficiently low ($T<<Tc$), the probability of spin-reversal processes (such as scattering by magnons or magnetic impurities) is small, as compared to other scattering processes in which spin orientations are conserved. Therefore, the electric current is carried independently by majority and minority electrons, and electrical conduction occurs for two separate spin channels in a parallel circuit.

Mott also pointed out that the scattering rates of up-spin and down-spin electrons are different in ferromagnetic metals. According to Mott, electric current is carried by electrons from *s* bands because of their high mobility and low effective mass. On the

other hand, localized *d* bands provide final states for the scattering of electrons. Due to the exchange interaction between *d*-band electrons in ferromagnetic metals, the majority and minority spin bands are split and shifted with respect to each other (Fig 2.1.7).

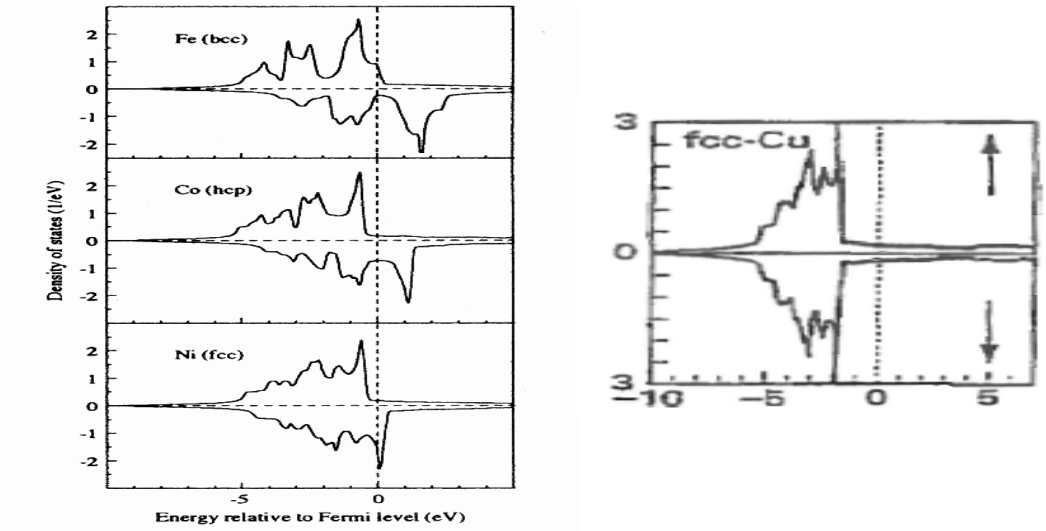

(i) (ii)

Fig. 2.1.7 Schematic view of band structures of Fe, Co and Ni (i) and Cu (ii).

Thus, the density of states at Fermi levels in majority and minority bands are different. As the probability of scattering is proportional to the density of states at Fermi level, the scattering rates are spin-dependent [15]. As a result, the resistivity of majority and minority spin electrons are different.

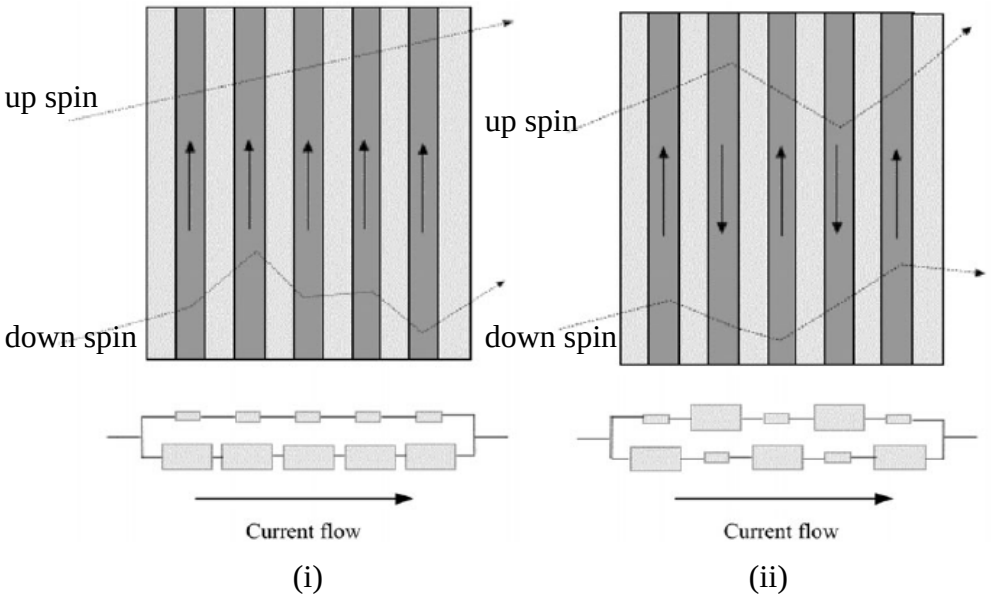

Fig. 2.1.8 Schematic illustration of electron transport in multilayer for parallel (i) and antiparallel (ii) magnetization configurations. Cartoons at the bottom of each figure show the resistor networks under the two-current series resistor model [16].

Based on the arguments mentioned above, the GMR effect in magnetic multilayers can be explained as follows. Figure 2.1.8 shows a magnetic/non-magnetic multilayered structure in parallel and anti-parallel configurations. For the magnetization of magnetic layers in parallel configuration (Fig 2.1.8(i)), one of the spin channels has electrons passing through the structure with less scattering. On the other hand, the opposite spin channel suffers more scattering. As the two spins channels do not mix strongly, electrical conduction occurs in parallel for two different spin channels. The total resistance of the multilayer is therefore low, due to shunting by the highly conductive

up-spin channel. When the magnetization of magnetic layers are in the antiparallel configuration (Fig 2.1.8(ii)), both the up and down spin electrons suffer from strong scattering because electrons of one spin channel (up or down) in one magnetic layer will become members of the other channel (down or up) as they enter the next magnetic layer. The total resistance of the multilayer is high in this case.

This scattering mechanism proposed by Mott is effective for bulk ferromagnetic materials, and is referred as the bulk spin dependent scattering. On the other hand, interfaces between ferromagnetic and non-magnetic materials also contribute to the spin dependent transport in magnetic multilayers [17]. For two adjacent materials with different band structures, a potential step can be created at the interface [17]. Thus, the transmission probability across the interface layer is reduced. Because the band structures of ferromagnetic materials are spin-dependent, the transmission across interfaces between ferromagnetic and non magnetic layer is also spin-dependent.

2.1.6.4 Spin valve

To achieve parallel and anti parallel configurations of the magnetic layers that can be switched with small magnetic fields, Dieny *et al.* [18] fabricated a 'spin valve' structure as shown in Figure 2.1.9(i). In such a structure, the two ferromagnetic layers are uncoupled from each other by using a relatively thick spacer layer (typically a few nm). To facilitate independent switching of ferromagnetic layers, exchange bias effect [19] was used. It was done by depositing an antiferromagnetic layer (pinning layer) adjacent to one of the ferromagnetic layers (pinned layer) in an external magnetic field. The magnetization of the pinned layer remains unchanged, until a large magnetic field is applied. The other ferromagnetic layer (free layer), having a much smaller coercivity, can then be switched with a much lower magnetic field. Figure 2.1.9(ii) shows the room temperature hysteresis loop and MR behaviour of a typical spin valve structure [18].

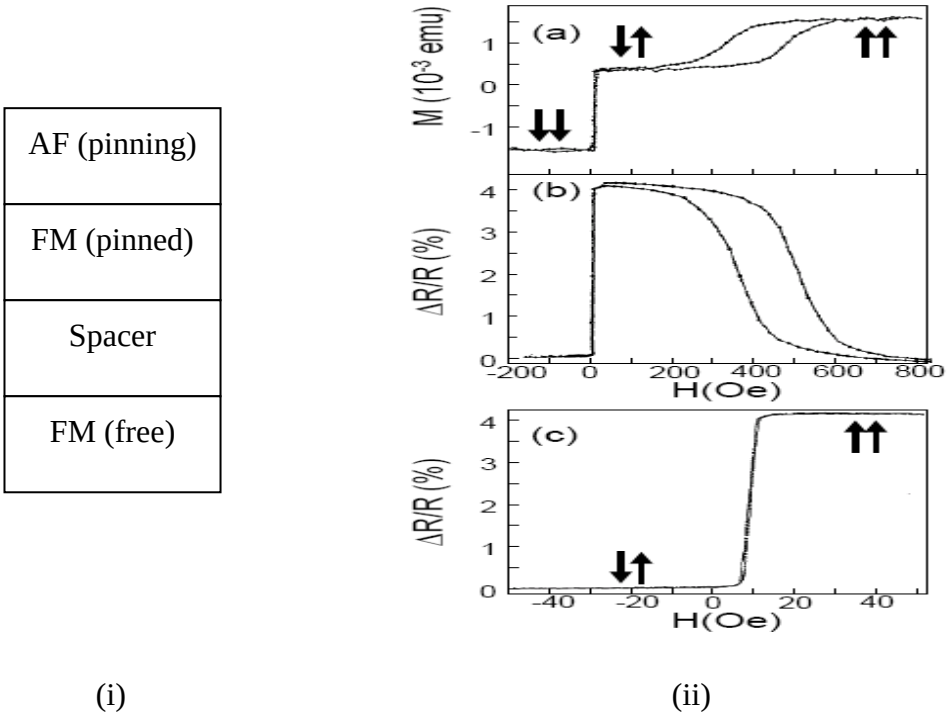

Fig. 2.1.9 (i) Schematic of a conventional spin valve structure. (ii) Hysteresis loop (a) and MR behaviour (b) of a spin valve sample Ta (5nm)\NiFe (6nm)\Cu (2.2nm)/NiFe (4nm)\FeMn (7nm)\Ta (5nm). (c) shows the MR when a minor loop was performed on the free layer. Measurements were performed at T = 300 K. [18]

A modified spin valve structure, which does not rely on the exchange bias effect to facilitate the independent switching of ferromagnetic layers, is shown in Figure 2.1.10. It works by using two magnetic layers with very different coercive fields. A magnetic field can be applied to reverse the magnetization of the soft layer before switching another layer (hard layer) which has a higher coercive field. This type of structure is called ‘pseudo spin valve’.

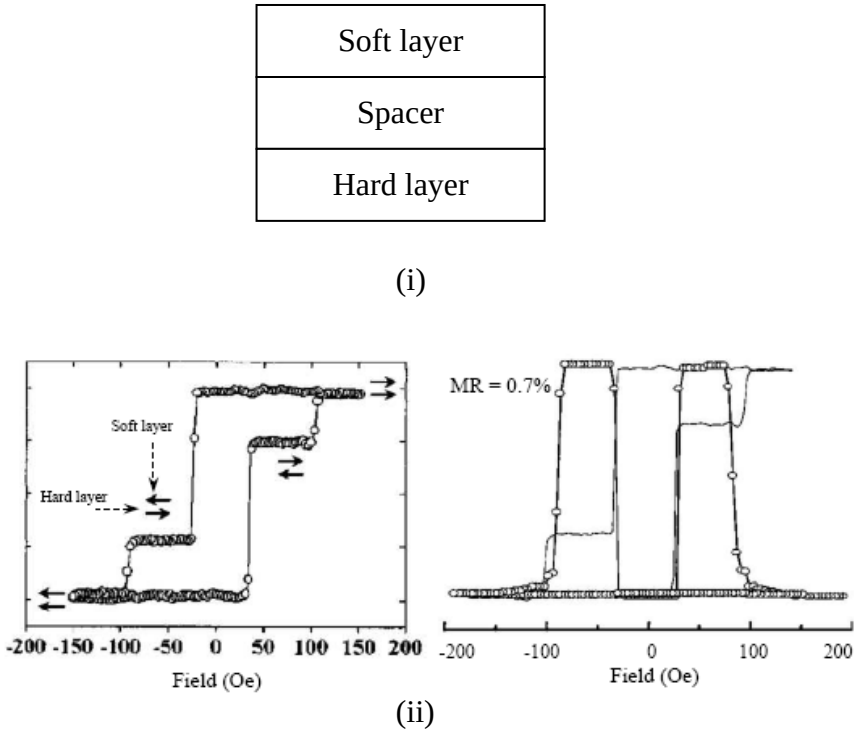

Fig. 2.1.10 (i) Schematic and (ii) magnetic and transport behaviour of pseudo spin valve structure: GaAs\Co (2nm)\Cu (6nm)\NiFe (6nm). [20]

A sharp M(H) loop implies a rapid change of MR with a small change in applied field, meaning a high sensitivity (resistance variation per unit change of magnetic field). In order to achieve high sensitivity, exchange coupling between the soft and hard layers should be minimized by critically controlling the spacer thickness. Various types of coupling, such as direct coupling through pinholes in the spacer, can destroy the MR effect [21]. Magnetostatic 'orange peel' coupling is another important source of

coupling. It arises from the generation of magnetic dipoles due to the films roughness (Fig. 2.1.11).

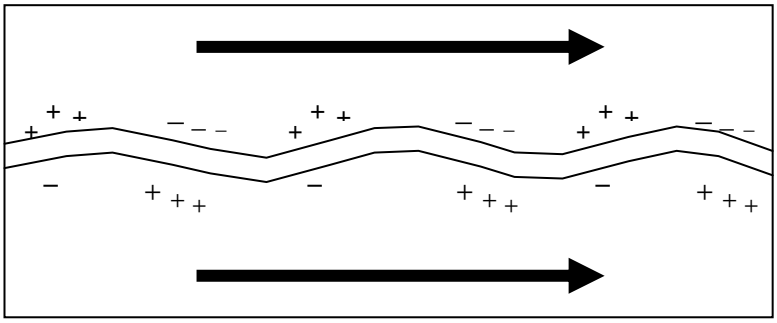

Fig. 2.1.11 Ferromagnetic coupling of magnetic layers due to formation of magnetic dipoles at rough interfaces.

2.2 Half metallic manganites

2.2.1 Introduction

In 1950, Jonker and Van Santen carried out studies on the compounds $La_{1-x}A_xMnO_3$ (A=Ca, Sr and Ba) [22, 23]. They reported a large increase of electrical conductivity as the mixed valence ratio of Mn^{4+}/Mn^{3+} increased (doping level $x = \frac{Mn^{4+}}{Mn^{3+} + Mn^{4+}}$). At certain values of x (=0.3) ferromagnetism was observed, which was accompanied by a sharp increase in electrical conductivity.

The research field was revived in 1993, when von Helmolt *et al.* reported a MR value ($\Delta\rho / \rho(H = 0)$) of 60% at room temperature in $La_{0.67}Ba_{0.33}MnO_3$ thin films under a 7-Tesla external field [24]. In 1994, Jin *et al.* reported MR values up to 1000% at 77 K in $La_{0.67}Ca_{0.33}MnO_3$ thin films under a 6-Telsa field [7]. Such kind of huge resistance changes under high magnetic fields is termed as colossal magnetoresistance (CMR).

2.2.2 Crystal and electronic structures

Mixed valence manganites $RE_{1-x}M_xMnO_3$ (RE = rare earths, M = Ca, Sr, Ba, Pb) are CMR materials with perovskite crystal structure (ABO_3) (Fig.2.2.1). The Mn ions occupy the B-sites with octahedral oxygen coordination. The MnO_6 octahedra share the corners to form a three-dimensional network. As interstitial A-site ions do not fit to maintain the cubic symmetry to MnO_6, it lowers the cubic symmetry and form orthorhombic perovskites (Fig 2.2.2).

Isolated Mn ions have five degenerated 3*d* orbitals. In the crystal form, the 3*d* orbitals are split by crystal fields and form three t_{2g} orbitals with lower energy and two e_g orbitals with higher energy (Fig 2.2.3). For Mn^{3+} ions, the t_{2g} orbitals are completely filled and one electron fills in the e_g orbital. All these electrons are aligned in parallel due to Hund's coupling. There is further orbital degeneracy lifting due to the Jahn-Teller effect which will be discussed later.

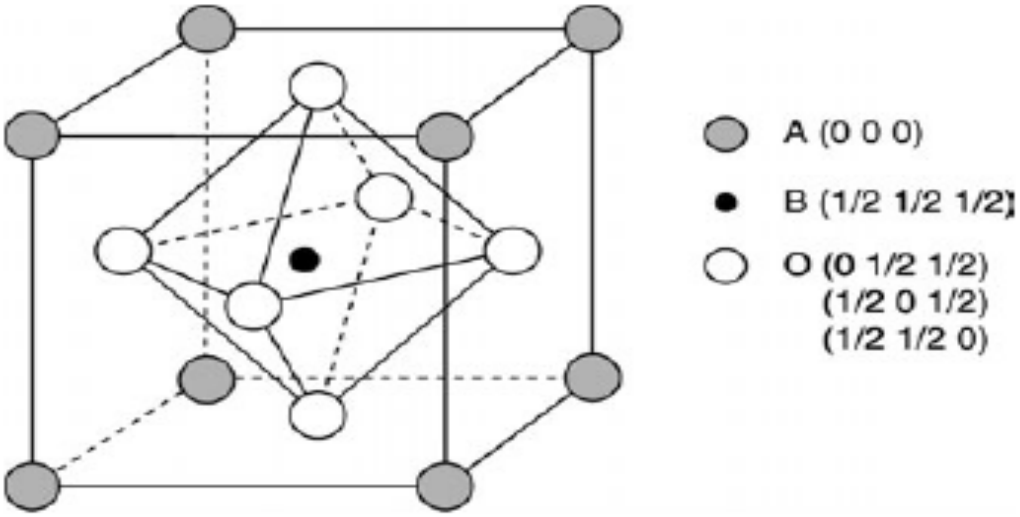

Fig. 2.2.1 Schematic of cubic perovskite structure. [25]

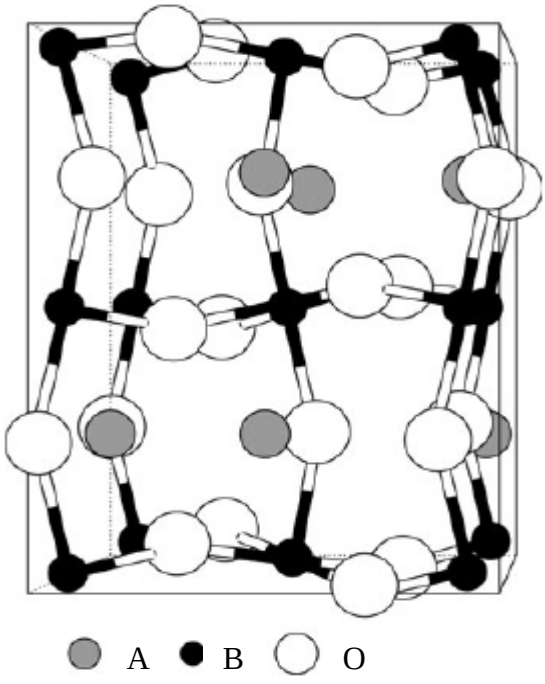

Fig. 2.2.2 Crystallographic structure of an orthorhombic perovskite. [25]

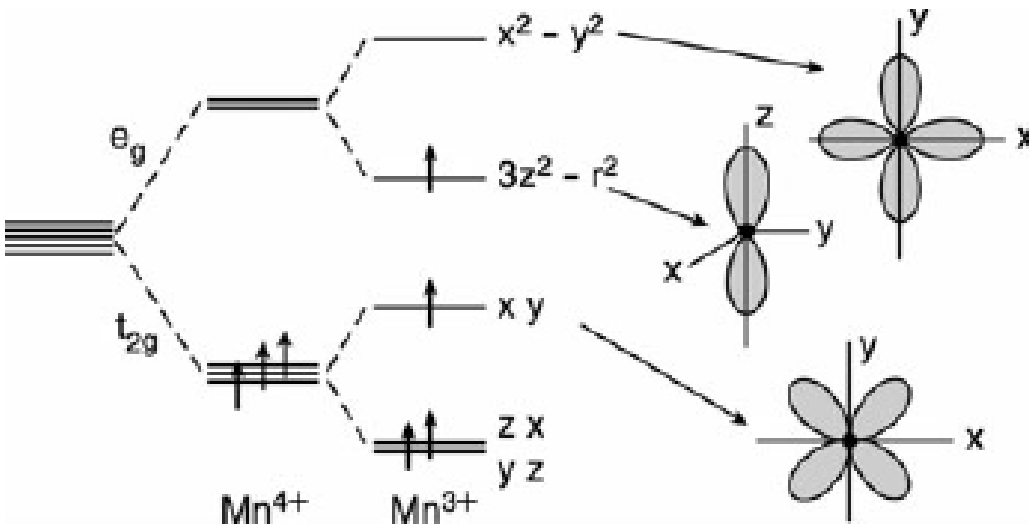

Fig. 2.2.3 Energy levels and orbitals of Mn^{4+} and Mn^{3+} due to the crystal field of octahedral symmetry and Jahn-Teller distortion effect. [25]

2.2.3 Electron-lattice interaction

Electron-lattice interactions can be divided into two types. The first type of interaction depends on the size of cations. In order to obtain cubic perovskite structure, ideal A-site cation radius is used [25]. If the radii of mixed cations are smaller than the ideal value, the MnO_6 octahedron is distorted. In perovskites, electron hopping is the main mechanism responsible for electrical conduction. For manganites, in particular, electron hopping is sensitive to the angle of the Mn-O-Mn bonds. As the bending angle increases, the hopping amplitude (and thus conductivity) is decreased. The effects of

doping level of A-site cations have been investigated by several groups. For example, the effect of A-site substitution by Y has been studied, and the result is shown in Figure 2.2.4 [26].

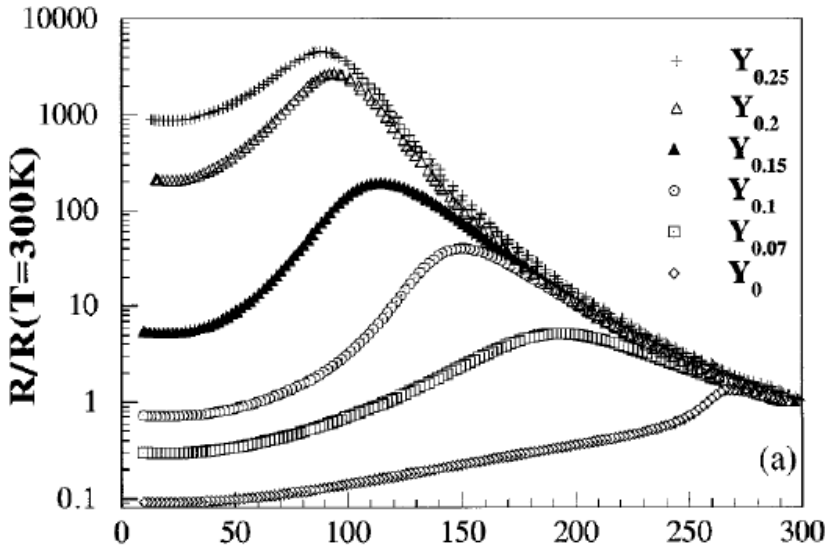

Fig. 2.2.4 Normalized resistivity, [R(T)/R(300K)] of a series of $La_{0.7-x}Y_xCa_{0.3}MnO_3$ (x=0, 0.07, 0.10, 0.15, 0.20, and 0.25) samples. The Mn-O-Mn bond angle deviates from 180° with increasing x. [26]

In the second type of electron-lattice interaction, MnO_6 octahedral are distorted by Mn^{3+} ions, whereas the Mn^{4+} ions preserve the cubic symmetry. The effect is called Jahn-Teller distortion [27]. In a Jahn-Teller distorted unit cell, local elongation or compression of MnO_6 octahedra along the z axis causes cooperative displacement of ions in the x-y plane, and the otherwise degenerate e_g orbitals are split into two (Fig.

2.2.3). When an e_g electron hops between adjacent Mn ions, the local lattice distortion is induced due to the presence or absence of the Jahn-Teller distortion. The coupling between e_g electrons and lattice distortion is known as polarons. [25]

2.2.4 Exchange interaction

The magnetic properties of manganites are controlled by exchange interactions between the net spins of Mn ions, which arises from the electrons. Apart from direct ferromagnetic exchange interaction, super-exchange and double-exchange interactions are also involved [28].

In the super-exchange interaction, t_{2g} electrons in Mn ions are localized due to the weak overlapping between t_{2g} orbitals and O-2*p* orbitals. The t_{2g} electrons interact with each other due to the virtual hopping between two Mn ions. As t_{2g} orbitals are half-filled for both Mn^{3+} and Mn^{4+} ions due to Hund's coupling, the spins of transferred electrons between Mn^{3+} and Mn^{4+} ions have to be of opposite signs according to Pauli Exclusion Principle. The relative spins of Mn^{3+} and Mn^{4+} ions are antiparallel, resulting in anti-ferromagnetic ordering.

In double-exchange interaction, electrons from the filled e_g orbital of Mn^{3+} ions are

transferred to O-2*p* orbitals. At the same time, electrons from O-2*p* orbitals are transferred to empty e_g orbitals of Mn^{4+} ions. This electron transfer process strongly depends on the t_{2g} spin orientation in the two Mn ions. When the localized t_{2g} spins of two Mn ions are aligned parallel, e_g electron transfer is possible with maximum kinetic energy. The probability of e_g electron transfer is $t_0 \cos(\frac{\theta}{2})$, where θ is the angle between Mn ion spins and t_0 is the hopping parameter [29]. Therefore, this double electron transfer process between Mn^{3+} and Mn^{4+} ions causes ferromagnetic ordering.

The schematic electronic band structure of Ni and doped $LaMnO_3$ in the ferromagnetic phase is shown in Figure 2.2.5. In 3*d* ferromagnetic metals such as Ni, both up and down-spin bands are occupied, leading to a partial (spin) polarization of conduction electrons. In manganites, however, the spin bands are separated by 1 eV or more, with the upper band above the Fermi level. It leads to a complete polarization of conduction electrons, or the so-called half metallic behaviour [30].

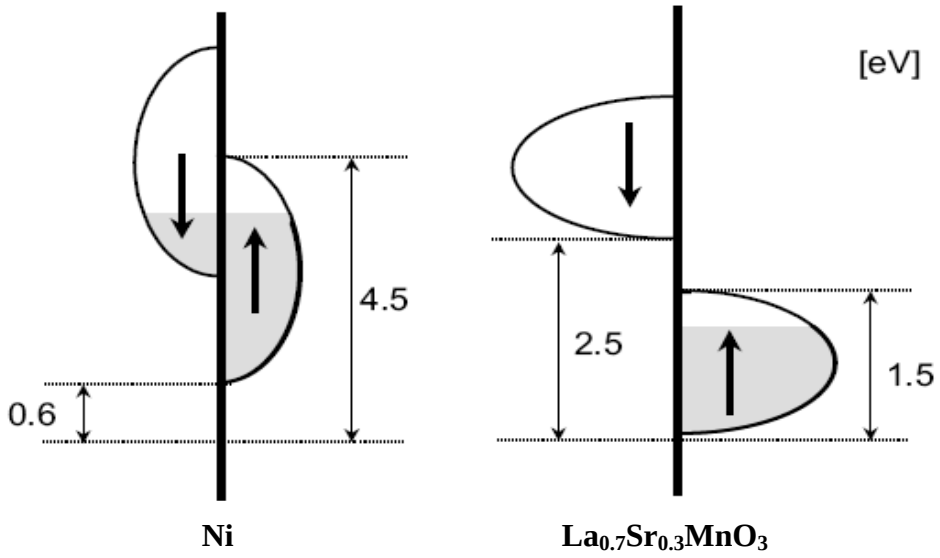

Fig. 2.2.5 Schematic view of band structures of Ni and LSMO [25].

2.3 Summary

This chapter introduced different types of magnetoresistances including ordinary MR, anisotropic MR, tunneling MR, colossal MR and giant MR. The concepts of half metallic manganites were also introduced as the background to understand the experimental work presented in Chapters 4 and 5.

CHAPTER 3

Experimental Methods

3.1 Pulsed laser deposition (PLD)

3.1.1 Introduction

After Dijkkamp first used the technique to prepare high temperature superconducting films in 1987 [31], PLD technique has gained tremendous interest and emerged as a versatile method to obtain epitaxial thin films of multi-component oxides. Various classes of materials, including ferroelectrics [32], ferromagnets [33] and dielectric oxides, have been grown successfully by the method, either as single layers or in multilayer form.

The basic principle of PLD is described as follows. Laser pulses are focused by converging lens. The pulses enter a vacuum chamber through a window and impinge on the target material. To ensure that only the surface layer of the ablated target is being heated up, laser pulses with energy density of a few Jcm^{-2} and short duration (~20 ns) are generally used. As thermal conduction cannot set in for such a short time scale, all of the absorbed energy is confined at the surface layer of the target. A few thousand

degrees Celsius can be achieved at the surface of the target [34].

3.1.2 Mechanism of PLD

The PLD process can be divided into four stages: (1) laser-target interaction, (2) dynamics of the ablated materials, (3) deposition of ablated materials on the substrate, and (4) nucleation and film growth.

In the first stage, focused laser pulses impinge on the target. All elements on the target surface are rapidly evaporated, and are ablated with identical stoichiometry as target material. The ablation process has a number of physical origins, including thermal, electronic, exfoliational and hydrodynamic. Thermal sputtering is the vaporization from a momentarily heated target. Electronic sputtering involves some forms of excitation or ionization such as production of electron-hole pairs, transition to anti-bonding potential energy on surface, lattice-localized relaxation and desorption from the surface. Exfoliation is the flake detachment from the target owing to repeated thermal shocks. Finally, droplets of materials can be formed and expelled from a target due to momentary melting [34].

In the second stage, ablated materials move towards the substrate according to laws

of fluid dynamics. The moving front of such a collection of particles form a luminous plasma called plume. The profile of the plume is described by a $\cos^n\theta$ curve, where n>>1 [35].

In the third stage, ablated high-energy species impinge onto the substrate surface and sputter some of the surface atoms away. A collision region is established between sputtered atoms from the substrate and incoming energetic species. This collision region serves as a source for the condensation of atoms. Films start growing at a time after the region is formed.

In the final stage, nucleation and growth of crystalline films occur. The process depends on several factors such as density and energy of ablated species, their degrees of ionization, substrate temperature, and physical-chemical processes occurring on the substrates. The nucleation and growth of films can be categorized into three different modes: (1) three-dimensional island growth (Volmer-Weber), (2) two-dimensional full-mono-layer growth (Frank-van der Merwe), and (3) two-dimensional growth of full monolayers followed by the nucleation and growth of three-dimensional islands (Stransk-Kastinov) [34].

3.1.3 Advantages of PLD

Films fabricated by PLD normally retain the stoichiometry of multicomponent targets, as long as there are no volatile species involved. It is due to the very high energy density of the focused laser pulses. Such energetic pulses can evaporate all the components in the target at the same time in spite of their different activation energies. In addition, the energetic species have sufficient kinetic energies to migrate to their favorable sites after landing on the substrates, which is further assisted by the high substrate temperatures. By using a rotating multi-target holder with suitable optical alignment, *in situ* growth of different materials under different ambient gas conditions is feasible.

3.1.4 Disadvantage of PLD

Some shortcomings for thin film deposition using PLD have been identified. There are two main problems: (1) inhomogenity of film thickness across the same sample, and (2) generation of particulates.

For a typical PLD system setup, due to the angular spread of the plume, reliable thickness calibrations can only be obtained around an area of 1 cm^2 directly under the

plume. Even so, the films are generally thicker right under the centre of the plasma plume, and the film thickness decreases with increasing distance from the plume center. The uniformity of film thickness can be improved by rotating the substrates during deposition [34].

Generation of particulates is also a common problem in PLD. The size of particulates can be as large as a few microns. The presence of particulates can greatly affect the growth of subsequent layers, and can jeopardize the usefulness of the films, especially in microelectronics applications [36]. To reduce the amount of particulates formed, a blocking mask can be placed in between the substrate and the target holder [34].

3.1.5 PLD setup

Figure 3.1 shows the configuration of the PLD system used in this project. In this PLD system, laser pulses were provided by a KrF Lambda Physik COMPex 200 excimer laser with wavelength 248 nm. Laser pulses (~20 ns) with energy in the range of 150 – 600 mJ could be produced by the laser. The cross sectional area of the beam was 1 cm × 3 cm as it left the laser. The maximum pulse repetition rate used for PLD

was 20 Hz. Laser-quality optical “UV-grade fused silica” windows and lenses were used in the PLD system, with a transmittance over 90 % for the wavelength range from 185 to 2000 nm. A focusing lens was used to achieve high laser fluence (~ 5 Jcm^{-2}) for target ablation. The focal length of the lens was 30 cm, matching the size of the chamber. To increase the flexibility of the PLD setup, two deposition chambers were installed served by the same excimer laser. The laser source was decoupled from the deposition chambers, and a beam steering mirror was used to direct the laser beam to either one of the two deposition chambers. To minimize propagation losses, multi-layered dielectric narrow-band high-reflection mirrors were used, with a reflectivity higher than 95 % at the wavelength 248 nm.

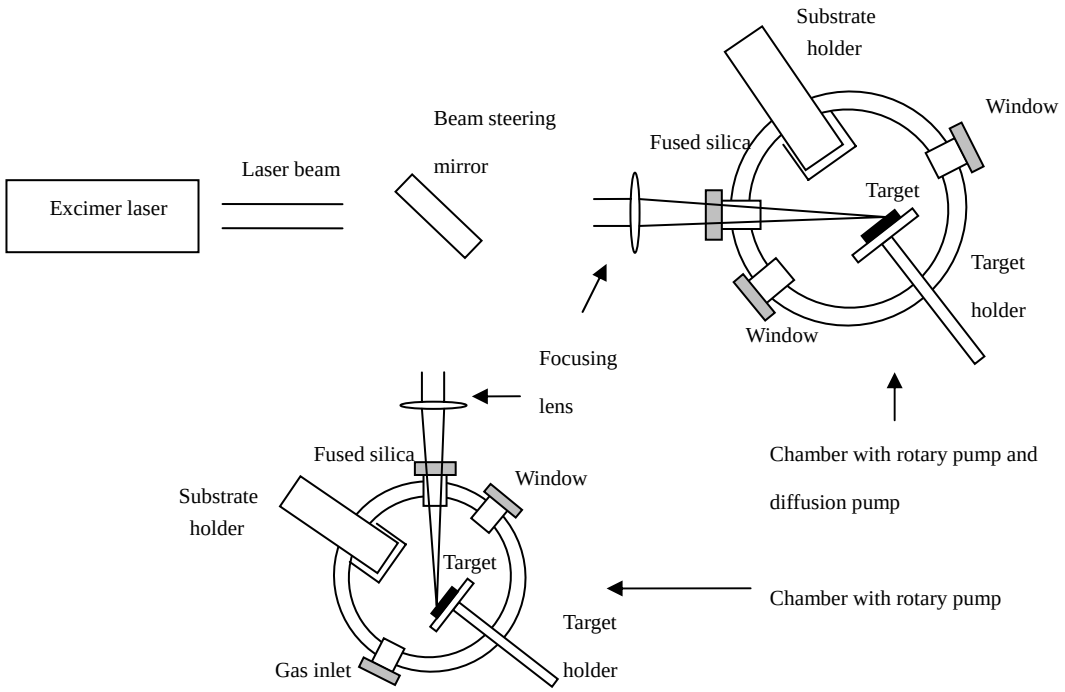

Fig. 3.1 Schematic diagram of a PLD system used in the project.

The PLD chamber used in this project consisted of the following components: 2 deposition chamber, target manipulator, substrate holder and heater, vacuum pump, gas supply and vacuum gauges. All vacuum chambers had ports for vacuum pumping, pressure gauging, targets, substrates, laser beam and viewports. One of the chambers was used for oxide film deposition, which was connected to a rotary pump. A gas inlet port was used for the afflux of oxygen (99.7 % purity), which provided an oxygen environment for oxide thin film fabrication. The chamber was pumped down to a base pressure of 1 mTorr. Afterwards, oxygen was filled into the chamber to the desired film

growth pressure. For metal film deposition, better vacuum deposition conditions were needed. In such a case, another chamber with diffusion pump was used to achieve the base pressure of 10^{-6} Torr.

To control the substrate temperature during film deposition process, a home-made substrate holder with diameter of 4 cm was used. It provided a stable substrate temperature up to 700 °C. Halogen quartz lamps, enclosed in a cylindrical stainless steel case, were used as heating elements. A type-K thermocouple was used for registering the temperature on the substrate holder, and the heating rate was controlled by a programmable controller. The substrates were mounted on the substrate holder with high temperature-compatible silver paste. Due to the high thermal conductivity of silver paste, a uniform temperature distribution across the substrates could be achieved.

3.2 Characterization and measurements

3.2.1 Structural characterization

3.2.1.1 X-ray diffractometry (XRD)

XRD is a non-destructive method for characterizing crystal structures of materials. When a x-ray beam interacts with the atoms in the material, the beam is diffracted.

Based on Bragg's law, diffracted beams constructively interfere only if they are at certain incident angles with the crystal planes. The Bragg condition,

$$2d\sin\theta = n\lambda \quad , \qquad (3.1)$$

shows the relation between x-rays wavelength λ, atomic plane separation d and the angle of incident beam θ, and n is an integer. That means each material produces a unique profile of x-ray intensity versus diffracted angle. From the diffraction pattern, we can determine the phases present in the sample, as well as crystallographic information, by comparing the XRD pattern to a library of known diffraction patterns.

An x-ray diffractometer consists of an x-ray source, slits of varying widths, a monochromator and a detector. X-ray is obtained by accelerating electrons to collide with a target (which was made of copper, for the system used in this project). Two relatively high-intensity radiations are emitted during the process: K_α and K_β. The average wavelength of the Cu K_α lines is 1.54 Å, and that of the Cu K_β lines is 1.39 Å. For obtaining a monochromatic x-ray beam, Ni foil was used to filter out the characteristic Cu K_β radiation, so that the peaks due to Cu K_β radiations were absent from the scans.

In the experimental geometry, there are four rotating axes of θ(ω), 2θ, χ and ϕ for

different scan modes (Fig. 3.2), as discussed below:

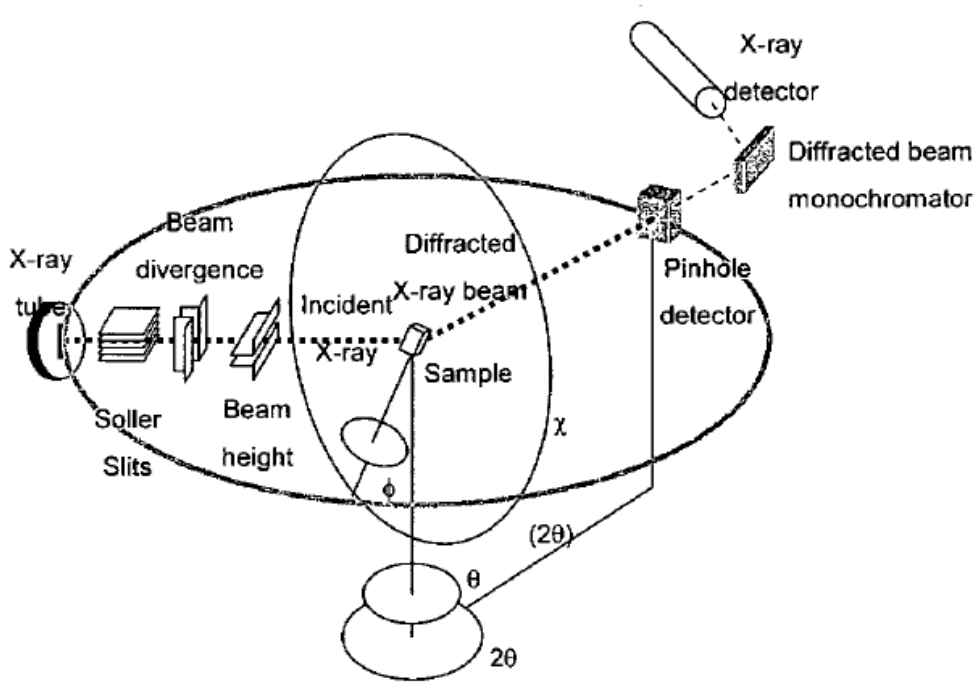

Fig. 3.2 Experimental geometry showing the four primary axes of a goniometer, the x-ray tube, detector and slits. [37]

- In a θ-2θ scan, the x-ray source is fixed, and the sample is rotated about an axis (ω -axis) that is normal to the plane containing the x-ray beam and the detector. The detector is rotated at twice the angular speed of the sample rotation, and the strongest signals is received for zeroth order (n=1) diffraction. θ-2θ scans can be used to determine the out-of-plane lattice parameters, and hence the crystalline phases present in the film and their crystallographic orientations.
- In a ω-scan, the x-ray and the detector are fixed, and the sample is rocked about the

ω-axis. The value of the full width at half maximum (FWHM) of the rocking curve reflects the degree of alignment among crystalline grains in the sample. Generally, a FWHM of around 1° is considered to be highly-oriented.

- In a ϕ-scan, the source and the detector are fixed at 2θ values corresponding to a specific atomic plane separation of the crystal structure. The sample is then tilted to a certain angle through the χ axis depending on the crystal structure. The sample is rotated about the ϕ axis that is normal to the sample stage. The ϕ scan can be used to determine the in-plane crystal structure, and the epitaxial relation between the film and the substrate.

  Using the cubic structure as an example, if the epitaxial relation of a thin film with cubic structure (with (100) out-of-plane orientation) is to be determined, the family of (100) planes of the film and the substrate should be selected for investigation. If the film is rotated by 45° through the χ axis (that is the line passing through the x-ray beam, sample stage and the detector), (101) planes diffractions can be obtained in θ-2θ scan. As the cubic structure has a four-fold symmetry in (101) planes, four peaks of $(10\bar{1})$, $(\bar{1}0\bar{1})$, $(\bar{1}01)$, and (101) planes separated by 90° can be observed in a 360° ϕ scan. If the four peaks of the film match to the peak positions

of the substrate, it can be concluded that the film is epitaxially grown, cube-on-cube, on the substrate.

3.2.1.2 Transmission electron microscopy (TEM)

TEM analyses were performed by using a JEOL 2010 system. The system used a LaB_6 electron source, and the electrons from the source were accelerated to 200 keV. Electrons were transmitted though an extremely thin specimen to form a diffraction image. The maximum magnification of the machine was 1.5 million times.

The TEM specimens were prepared by mechanical grinding and ion milling. Firstly, thin film samples were cut into two small rectangular pieces of 3×3 mm^2. Two film surfaces were stuck together, face to face, by means of G-1 epoxy. The specimen was then grinded mechanically to around 1 mm in thickness by using a series of abrasive papers with particle size ranging from 100 μm down to 20 μm. The grinded surface was then polished by using diamond polishing films with particle sizes of 6 μm, 3 μm, and 1 μm. After polishing one side of the specimen, the polished side was stuck on a 3 mm diameter copper supporting grid. The other side was then polished with the same procedures, until the silicon substrate turned red under an optical microscope operating

in the transmission mode. This indicated the thickness of the sample was around a few microns. The thickness of the specimen was further reduced by using Ar ion milling. A Gatan PIPS machine was used and operated at 4 kV. The specimen was milled until a hole was formed at the sample. The beam energy was then reduced to 2 kV to minimize the amorphous structures induced by high energy Ar ion bombardment.

3.2.1.3 Atomic force microscopy (AFM)

The surface morphology of thin film samples were studied by AFM operating in tapping mode. The technique gives detailed information about properties such as surface roughness and average grain size of the films. The working principle of AFM is based on the inter-atomic forces between the tip and the atoms in the sample. The schematic diagram of an AFM is shown in Figure 3.3.

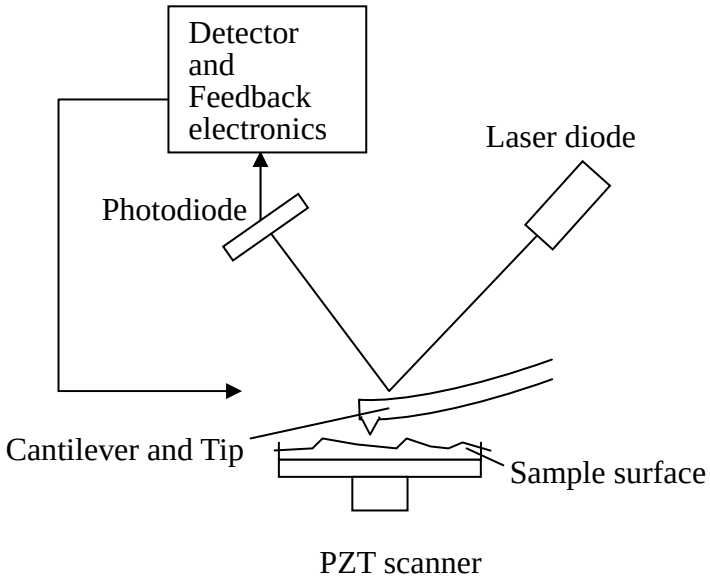

Fig. 3.3 Schematic diagram of an AFM.

The tip is tapped over near, but not touching, the surface of a film at the cantilever's resonance frequency. Due to the attractive inter-atomic forces between the tip and the film surface, some energy is lost to the surface, and the amplitude of oscillation is reduced. When the tip is high, the oscillation amplitude becomes large, and vice versa. A feedback loop constantly adjusts the separation between the tip and the sample. As the typical spring constant for cantilever is about 1 N/m, a deflection as small as 1 nm can be sensed when the force as low as 10^{-9} N is present between the film and the tip. Such a small deflection can be measured by the shift of the laser beam

image reflected off a shiny surface on the back of the cantilever. Nanoscale movement of the scanner is made by a piezoelectric scanner. Vibration isolation table is equipped to minimize the noise induced from the surrounding.

3.2.2 Magnetic measurements

The follow equation shows the relation between magnetic flux density (*B*), magnetic field intensity (*H*) and magnetization (*M*).

$$B = \mu_0 (H + M) \tag{3.2}$$

When a known external field *H* is applied to a vibrating sample, the change of flux density *B* inside the sample can arise from the change in magnetization. As the sample is vibrated, *B* inside the sample will generate an induced voltage in the pick-up coils according to Faraday's law,

$$\varepsilon = -\frac{d\Phi}{dt} = \frac{\partial}{\partial t}(\int B \cdot dS) \tag{3.3}$$

where Φ is the flux through the coils and *dS* is an element of vector area.

The magnetic properties of the samples were measurement by using a LakeShore model 7407 vibrating sample magnetometer (VSM) system. Figure 3.4 shows the schematic diagram of a VSM system. For the system used in this project, samples were

mounted on a sample rod, and were placed at the center of a pair of pickup coils between the poles of an electromagnet. The sample to be measured was then vibrated vertically by a head drive at 82 Hz. As the sample was vibrated, the magnetic flux passing through pick-up coils varied continuously. Thus, a voltage was induced and subsequently detected as the signal from the magnetic sample. By using a specimen of known magnetization to calibrate the VSM, absolute values of magnetic moments of any sample can be obtained. In our VSM, only the component of the moment parallel to the direction of the applied field can be measured. It is because the orientation of the pick-up coils was fixed in the direction parallel to the applied magnetic field.

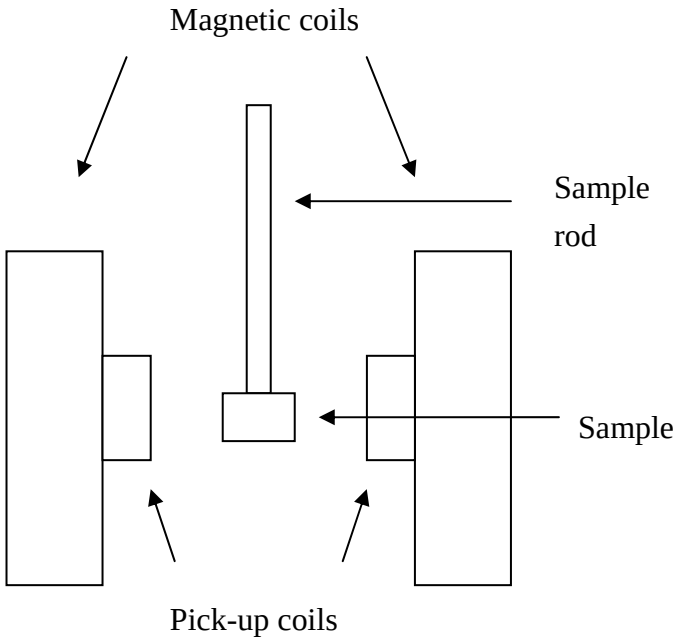

Fig. 3.4 Schematic diagram of a VSM.

The VSM was equipped with a cryostat for low temperature measurements from 4.2 K to 450 K. Liquid helium or nitrogen was continuously fed through a vacuum-jacketed transfer line to a vaporizer at the bottom of the cryostat chamber. Vaporized liquid was heated up to the specified temperature and traveled upwards along the sample space to cool the sample.

3.2.3 Electrical transport measurements

3.2.3.1 Resistance against temperature measurement

In electrical measurements, platinum contact pads were deposited on the samples through a stainless steel mask by PLD methods. Figure 3.5 (i) shows the pattern of the mask. Four copper wires were attached on the platinum pads using silver paste. The sample was then attached on the cold finger of the cryostat by thermal grease for better thermal conduction.

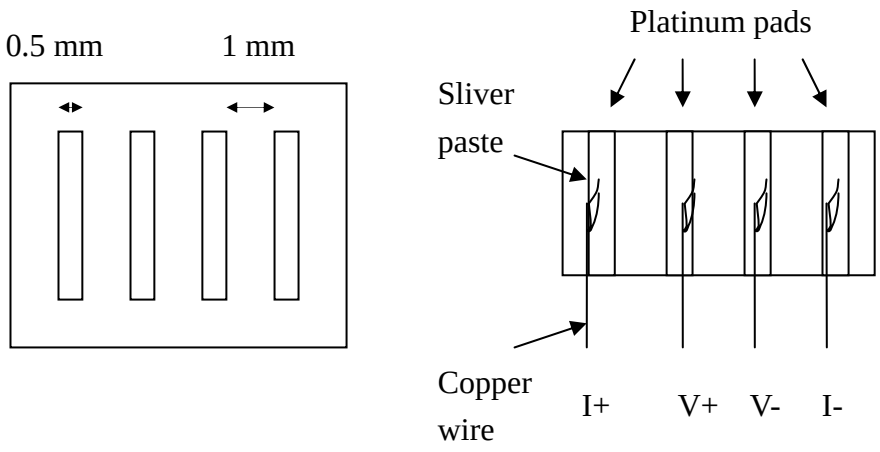

Fig. 3.5 (i) Pattern of mechanical mask with 0.5mm rectangular strip with equal spacing of 1mm. (ii) Configuration of resistance measurement.

A Keithley 2400 sourcemeter was used for resistance measurements. It has two pairs of

terminals for four point resistance measurements. By using four point measurements, the issue of contact resistance was minimized. Figure 3.5(ii) shows the configuration for such measurements. The measured resistance *R* was used to calculate the resistivity ρ by using the Equation 3.4,

$$\rho = \frac{RA}{l} \qquad (3.4)$$

where *l* is the distance between the current contacts and *A* is the cross sectional area that the current flows through.

A closed-cycle refrigerator was used to cool the sample to desired temperatures. Samples were cooled by a cold finger through direct thermal contact. A temperature controller was used to measure the temperature of the cold finger and to regulate the heater, maintaining the cold finger at the desired temperature. The temperature can be varied between 10 K to 400 K. Both the temperature controller and the sourcemeter were operated through a LabView program. The data were taken through the computer, and the graph of resistance against temperature (RT) was obtained.

3.2.3.2 Current against voltage

Current against voltage (IV) measurements were also done by Keithley 2400 sourcemeter. The configuration of measurement was the same as Figure 3.5 (ii). The whole measurement setup was computer controlled by a LabView program.

3.2.3.3 Resistance against magnetic field

Magnetoresistance measurements were measured in a system built in-house. The magnetoresistance measurement setup consisted of five parts: (1) electrical circuit (with sourcemeters and the sample), (2) an electromagnet, (3) a gaussmeter, (4) a closed-cycle cryostat and (5) a temperature controller. The schematic diagram of the MR setup is shown in Fig.3.6.

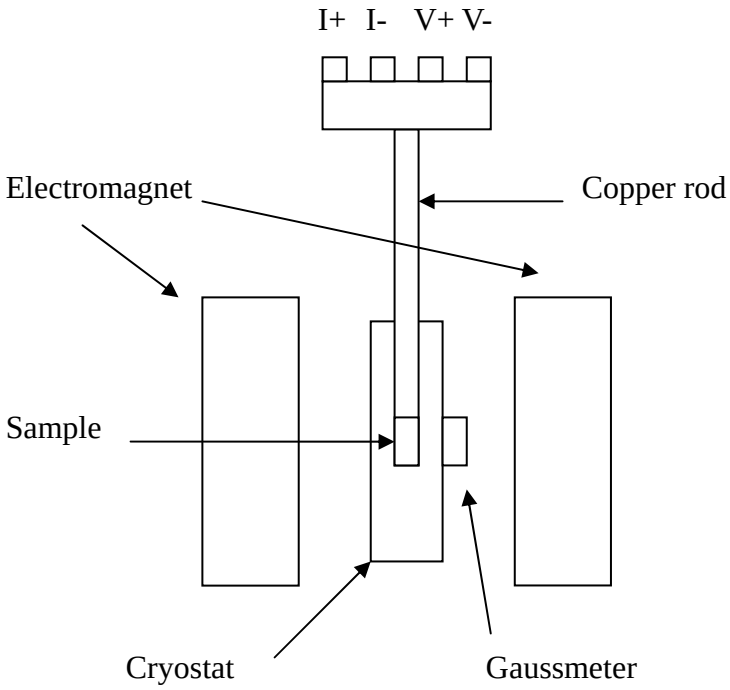

Fig. 3.6 Schematic diagram of the MR setup used in the project.

Due to the limited space of the cryostat, the maximum size of the sample that could be accommodated was 3 mm × 3 mm. The sample was mounted on a printed circuit board (PCB), and four aluminum wires were bonded between the sample and the PCB by ultrasonic wire bonding. The PCB was then mounted on a hollow copper rod with four copper wires inside for electrical connection. The sample rod was inserted into the cryostat between the poles of the electromagnet. The chamber and the vacuum jacket were evacuated by a rotary pump for 30 minutes. Then, helium gas was filled into the chamber for thermal conduction. The temperature controller was used for regulating the

temperature inside the chamber from 10 K to room temperature. The electromagnet provided a variable magnetic field up to 5000 Oe, which was measured by a gaussmeter adjacent to the cryostat. The resistance of the sample was measured by using four point measurement technique. All instruments were computer controlled by a LabView program.

CHAPTER 4

Effect of Post Annealing on $La_{0.7}Sr_{0.3}MnO_3$ Thin Films

4.1 Introduction

Doped perovskite manganites such as $La_{0.7}Sr_{0.3}MnO_3$ (LSMO) are heavily studied for spintronics applications, due to their high spin polarization and, particularly in LSMO, relatively high Curie temperature (T_C > 370 K) [38]. According to the double exchange theory [29, 28], ferromagnetic and metallic properties of perovskite manganites are inter-related through the interaction between pairs of Mn^{3+} and Mn^{4+} ions. Because the ratio of Mn^{3+} and Mn^{4+} ions can be altered by oxygen content, T_C of LSMO films can be modified by controlling oxygen pressure during the deposition process [39].

In multilayer fabrication processes, different growth conditions may be required for the deposition of individual layers. Chemical stability of the layers has to be carefully studied, ensuring that desired properties of individual layers are retained. For example, Dho and Hur [39] showed that LSMO films deposited at different oxygen pressures (varied from 250 mTorr to 450 mTorr) and annealed at 500 mTorr possessed

induced lattice strain. Sun *et al.* [40] showed that the transport behaviour of LSMO films strongly depended on the oxygen stoichiometry; their results showed that oxygen vacancies in LSMO films could induce scattering and affected the resistances of samples. Du *et al.* [41] reported that high temperature annealing of LSMO films at 950 °C in flowing oxygen at atmospheric pressure (deposited at 800 °C) could increase T_C and saturation magnetization of the films, and coercivity of the films was reduced at the same time. It should be noted that these works concentrated on oxygen-deficient LSMO films annealed *in situ* under high oxygen pressures and temperatures.

On the other hand, there are situations in which *ex situ* annealing of films are necessary. For example, mechanical masks are occasionally used to deposit films of specific geometries. In the absence of *in situ* loading mechanisms, the films need to be cooled down to room temperature and exposed to air for placing the mask into the chamber. As mentioned before, the oxygen content of LSMO films strongly depends on annealing conditions, so the film properties can be changed during the process.

In this work, I investigated the effect of post annealing on the properties of LSMO films, focusing on the effects of *in situ* and *ex situ* annealing processes under oxygen pressures different from deposition pressures. For *in situ* annealing experiments, films

were deposited at desired oxygen pressures and subsequently annealed. For the case of *ex situ* annealing, films were first deposited at desired oxygen pressures and cooled down to room temperature subsequently. Afterwards, the films were heated up again and maintained at an oxygen pressure different from that used for the deposition process. Results obtained in this chapter provide useful guidelines for the epitaxial multilayer deposition and annealing processes.

4.2 Fabrication and structural characterization of LSMO target

A LSMO target was fabricated by standard solid-state reaction procedures [42]. Table 4.1 shows the chemicals used, and the corresponding weight ratios of chemicals in the target.

	La_2O_3	$SrCO_3$	MnO_2
Molar weight (g)	114.16	44.74	86.95
Desired weight(g)	5.71	2.24	4.35

Table 4.1 Required chemicals and their weight

Powders of La_2O_3, $SrCO_3$ and MnO_2 were weighed according to the desired stoichiometric ratios in Table 4.1 and were mixed with ethanol. The mixture was ball milled for 10 hours, and then calcinated at 1200 °C for 10 hours to complete the chemical reaction. The calcinated powder was grinded into fine powder and compressed to a 3-mm thick circular pellet of diameter 2.5 cm by an oil compressor, under a force of 3.5 Ton. Finally the pellet was sintered at 1320 °C for 10 hours.

The as-prepared LSMO target was structurally characterized by XRD. Its chemical

composition was verified by EDX. In the θ-2θ scan shown in Fig 4.2.1, the peaks match well with that of rhombohedral LSMO listed in the International Centre for Diffraction Data (ICDD) database.

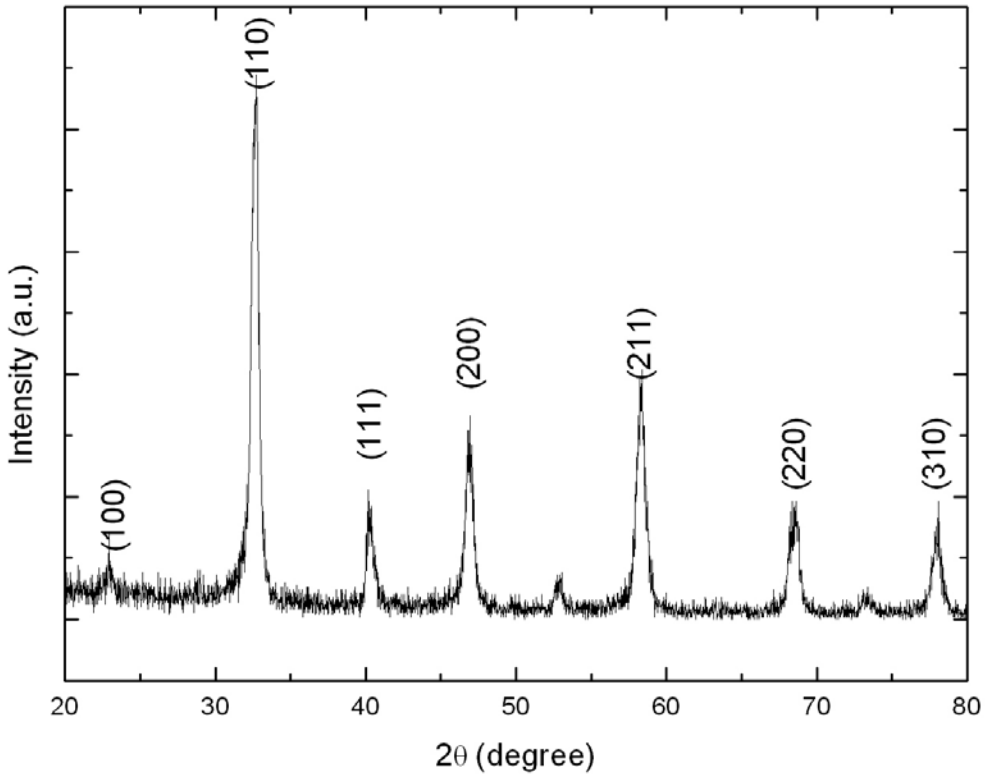

Fig. 4.2.1 XRD pattern of LSMO target.

4.3 Fabrication of LSMO thin films

The lattice mismatch between film and substrate materials can influence the lattice parameters of the deposited films, as well as their crystallinity and in-plane epitaxial relations. In this thesis, the lattice mismatch *f* is defined as the percentage difference in the lattice parameters of film and substrate materials:

$$f = \left(\frac{a_s - a_{bulk}}{a_s} \right) \times 100\%$$

where a_{bulk} and a_s are lattice constants of the bulk material and the substrate, respectively.

LSMO has a pseudo-cubic structure with lattice parameter a = 3.87 Å. Lanthanum aluminum oxide $LaAlO_3$ (LAO), a single-crystal substrate material used in the work, also possesses a pseudo-cubic structure with lattice parameter 3.79 Å, implying a lattice mismatch of -2.2 % with LSMO. Strontium titanate $SrTiO_3$ (STO) is another suitable substrate material because of a small lattice mismatch with LSMO (0.81 %). In this work, LAO was primarily used as the substrate material, and the epitaxy of films was generally comparable with LSMO films deposited on STO substrates under identical conditions in our PLD system.

LSMO thin films were deposited on LAO (100) substrates by PLD method. A laser

fluence of 3.6 Jcm^{-2} and frequency 5 Hz was used for the deposition process. The chamber base pressure during the deposition and post-deposition annealing processes was 5 mTorr. During the film deposition process, oxygen was filled into the chamber and maintained at a pressure of 150 mTorr, when the substrate temperature was gradually raised to 650 °C. The substrates were then annealed for 10 minutes before ablation started. The thicknesses of the films were controlled by the deposition time, according to a calibration rate of ~20 nm/min (the rate was obtained by examining the cross-section of a thick calibration sample, deposited for a specific duration of time, under the scanning electron microscope). LSMO thin films of thickness ~50 nm were deposited. The deposition parameters are summarized in Appendix A (table A).

4.4 Structural and electrical characterization of LSMO thin films

Figure 4.4.1 shows the θ-2θ scan of a 50-nm thick LSMO film grown on LAO (100) single crystal. The (h00) peaks are observed, indicating a textured growth of LSMO film on LAO. Figure 4.4.2 shows the rocking curve about the (200) peak, and the narrow peak (FWHM = 0.35°) suggests that the film was highly textured. To confirm epitaxial growth of the film, XRD ϕ-scans were performed. Figure 4.4.3 shows the ϕ-scans of LSMO (202) and LAO (202). Each of the LSMO (202) and LAO (202) profiles show four diffraction peaks separated by 90°. The four-fold symmetry confirms the cubic structure of LSMO thin film and LAO substrate. More importantly, the four peaks of LSMO are sharp and their corresponding ϕ angles match to the peaks of LAO. These indicate that the LSMO film was cube-on-cube grown on the LAO substrate.

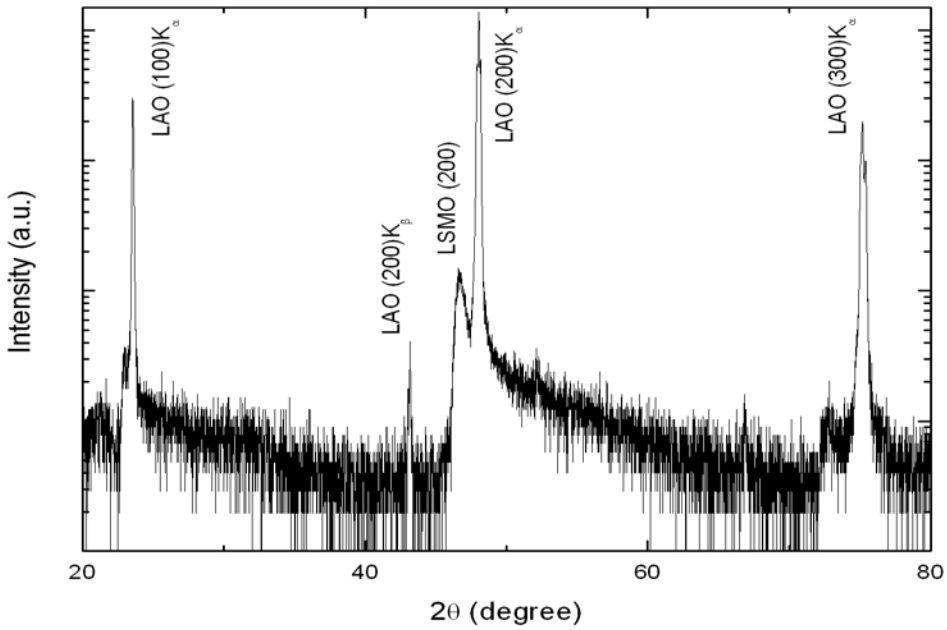

Fig. 4.4.1 XRD θ-2θ diffraction pattern of a 50-nm thick LSMO film deposited on LAO (100) substrate.

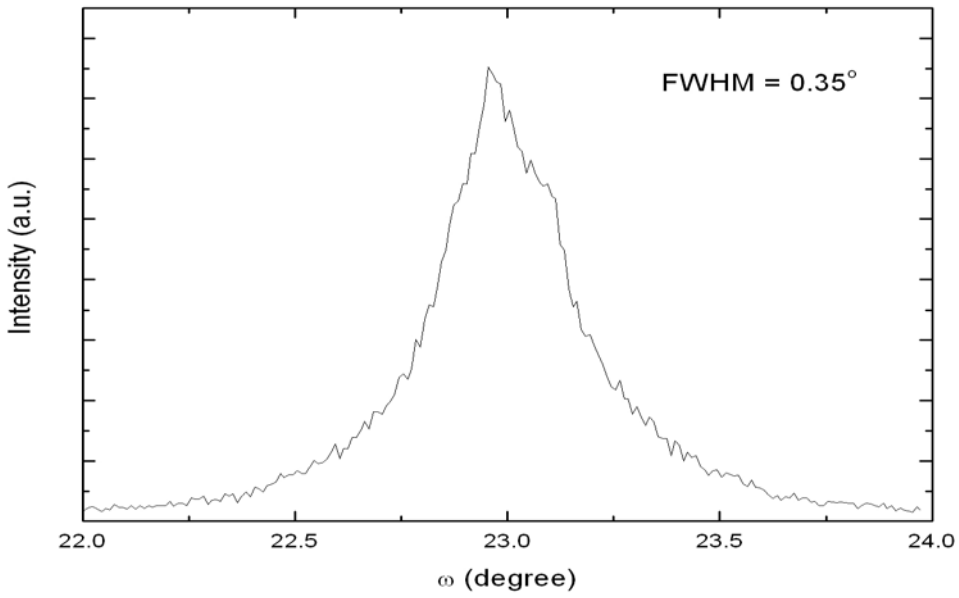

Fig. 4.4.2 XRD rocking curve about the (200) peak of the LSMO sample in Fig. 4.4.1.

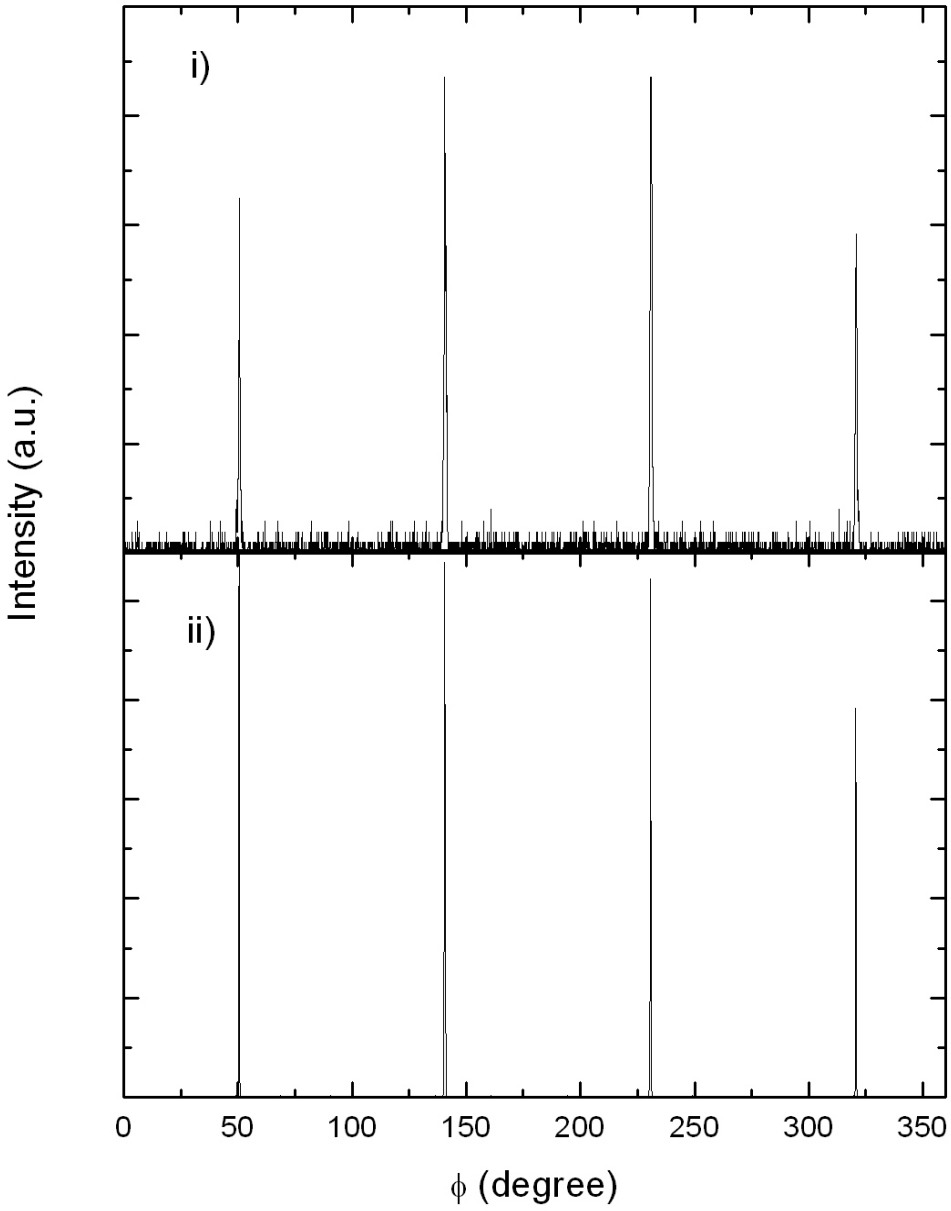

Fig. 4.4.3 ϕ-scan of the LSMO sample in Fig. 4.4.1. i) LSMO (202) and ii) LAO (202) planes.

Electrical resistances of the films were measured from 20 K to 380 K. Four rectangular-shaped gold electrodes were deposited on the films by sputtering through a mechanical mask. The peaks of resistance against temperature (R-T) curves were used to estimate the *Tc* of the films [43]. Figure 4.4.4 shows the R-T curve of a LSMO film fabricated under the same condition as the sample in Figs. 4.4.1 – 4.4.3, which exhibits a transition from metallic-like to semiconducting-like resistance behaviour. The measured *Tc* (from the peak of the R-T curve) was 350 K.

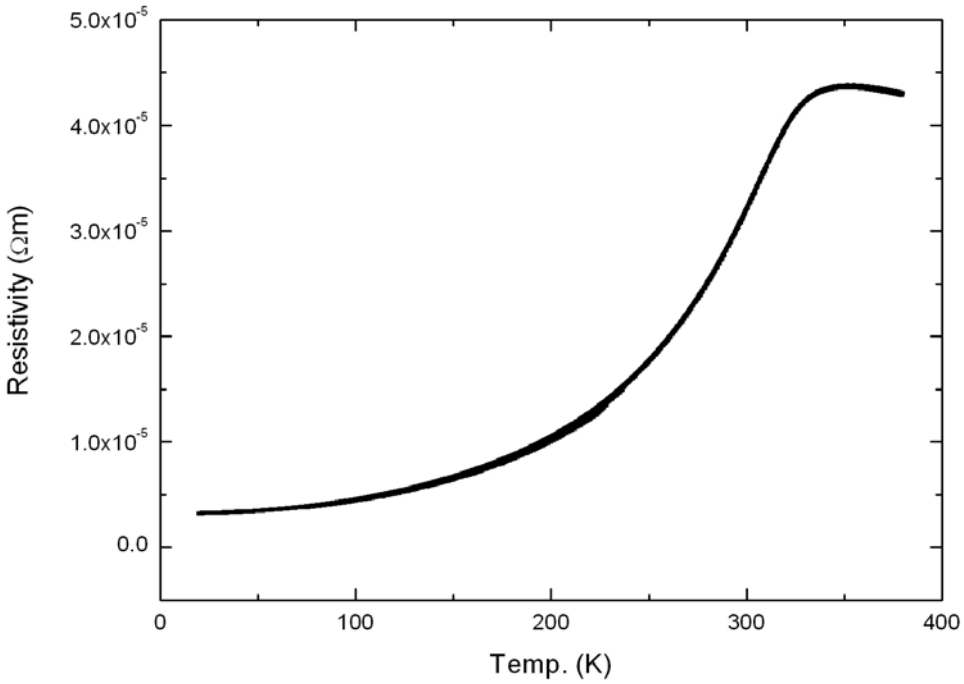

Fig. 4.4.4 Resistance against temperature relation of a LSMO film deposited at 650 °C under150 mTorr oxygen pressure.

4.5 *In situ* post annealing

Table 4.1 summarizes the *in situ* post annealing procedures. For the *in situ* post annealing study, films were deposited either at 150 mTorr (method 1) or 100 mTorr (method 2). Without switching off the heater, the deposited films were post-annealed at 100 mTorr (method 1) or 150 mTorr (method 2) for different durations. After annealing, the films were cooled down to room temperature naturally at the corresponding annealing oxygen pressures.

Procedures	Method 1			Method 2		
	Temp. (°C)	Oxygen Pressure (mTorr)	Duration (minutes)	Temp. (°C)	Oxygen Pressure (mTorr)	Duration (minutes)
Pre annealing	650	150	10	650	100	10
Deposition	650	150	2.5	650	100	2.5
Post annealing	650	100	10/20/30	650	150	0/5/20
Cooling	650→ R.T.	100	~60	650→ R.T.	150	~60

Table 4.1: Annealing procedures for *in situ* post annealing processes. R.T. refers to room temperature.

Resistances of the films were measured in the temperature range from 150 K to 380 K. Four rectangular-shaped gold electrodes were deposited on the films by sputtering through a mechanical mask. Peaks of resistance against temperature curves were used to estimate the Curie temperatures of the films [43].

Figure 4.5.1 shows the resistance against temperature plots of LSMO films grown on LAO at 150 mTorr and then annealed at 100 mTorr for different durations (method 1). As the post annealing time increased from 0 to 30 minutes, the Curie temperature of LSMO films increased from 330 K to 365 K. The control sample that was cooled down immediately after deposition in an oxygen pressure of 150 mTorr is shown in Fig. 4.5.1 (curve e), which had a higher resistance compared with the annealed films (curve a-d). One of possible reasons for the observation is the diffusion of oxygen out of the films, when the oxygen pressure was changed to 100 mTorr. As a result, the ratio Mn^{4+}/Mn^{3+} decreased and ferromagnetic ordering was reduced. However, other possibiliies exist, such as crystallinity changes [40] and strain relaxation [39] during the annealing processes, which can affect the T_C. Dho *et al.* [39] reported the results of x-ray diffraction (XRD) measurements for films that were deposited at 750 °C under different oxygen pressures (250, 350, and 450 mTorr) and post annealed at 750 °C in an oxygen

pressure of 500 mTorr for 30 minutes. As the oxygen pressure increased from 250 mTorr to 450 mTorr, T_C changed from 300 K to 360 K. The compressive lattice strain of the films was relaxed, and the out-of-plane lattice constant was decreased by 0.02 nm. In order to detect any changes in the lattice structures, I have performed XRD measurements on all of the film. The changes, if any, were too small to be detected in this experiment.

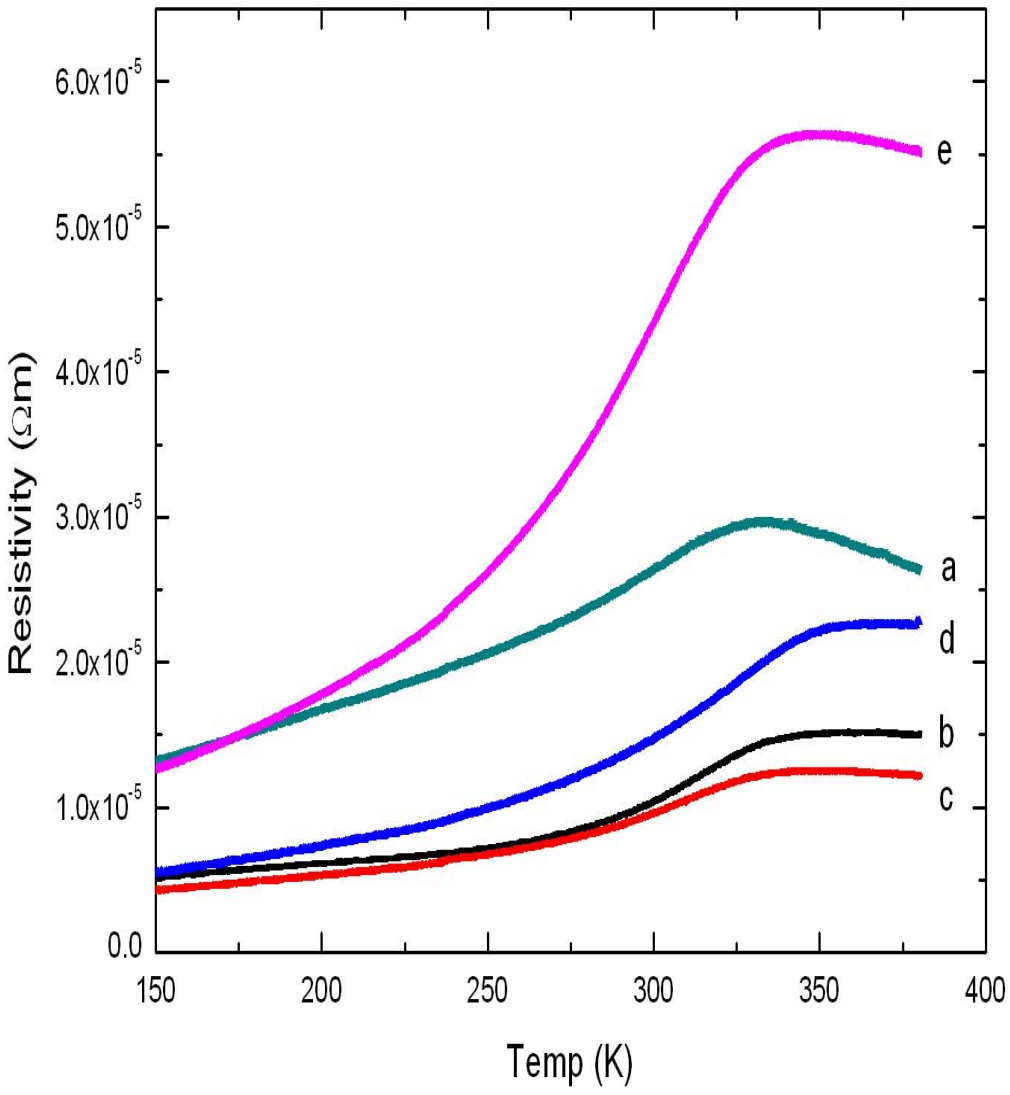

Fig. 4.5.1 Resistance against temperature curves of the films prepared by method 1 in Table 4.1, with different annealing times: (a) 0 minute (b) 10 minutes (c) 20 minutes (d) 30 minutes (e)without post annealing (cooling under 100 mTorr after deposition for curve a-d, and cool down without changing oxygen pressure for curve e)

Fig. 4.5.2 shows the resistance against temperature plots of films grown on LAO at 100 mTorr and annealed at 150 mTorr for different durations. All the films showed semiconducting behaviour from 150 K to 380 K, as evidenced by the negative slopes of the curves. During the annealing process at high oxygen pressure, the ratio of Mn^{4+}/Mn^{3+} can be increased by oxygen absorption since the films were oxygen deficienct during the deposition process. From the curves, no significant peak can be observed. But based on the semiconducting behaviour from 150 K to 380 K, the T_C of the films (if any) should be below 150 K.

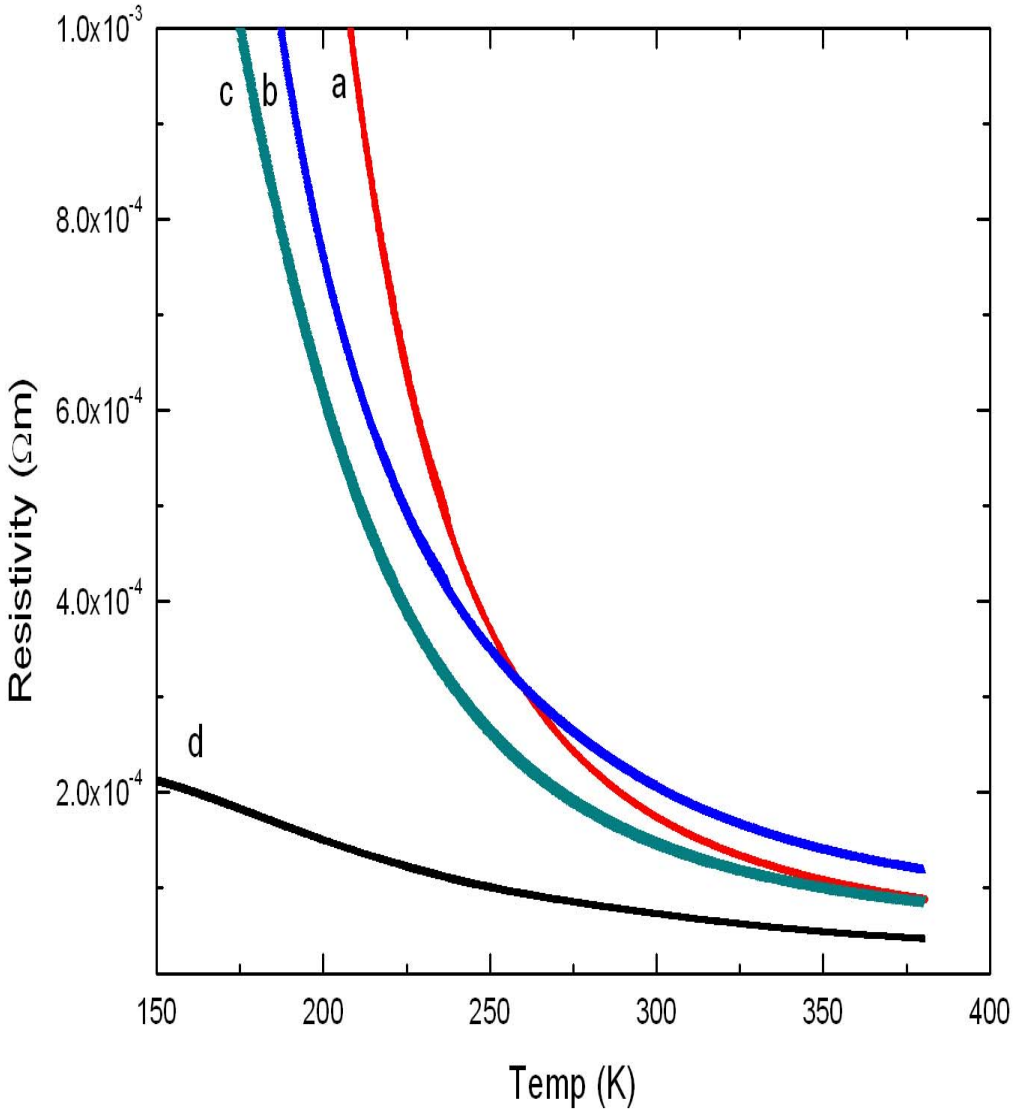

Fig. 4.5.2 Resistance against temperature curves of the films prepared by method 2 in Table 4.1, with different annealing times: (a) 0 minute (b) 5 minutes (c) 20 minutes (d) without post annealed (cooling under 150 mTorr after deposition for curve a-c, and cool down without changing oxygen pressure for curve d)

4.6 *Ex situ* post annealing

Table 4.2 summarizes the procedures for *ex situ* post annealing experiments performed in this project. For the *ex situ* post annealing study, films were deposited at 150 mTorr and cooled down to room temperature naturally at the same oxygen pressure. Then the films were heated up to 650 °C without (method 3) or with (method 4) oxygen filled into the chamber and annealed for different durations. Finally, the films were cooled down to room temperature with the oxygen pressure maintained at 150 mTorr. Resistances of the films were then measured in the temperature range from 150 K to 380 K.

Procedures	Method 3			Method 4		
	Temp. (°C)	Oxygen Pressure (mTorr)	Duration (mins)	Temp. (°C)	Oxygen Pressure (mTorr)	Duration (mins)
Pre-annealing	650	150	10	650	150	10
Deposition	650	150	2.5	650	150	2.5
Cooling	650 → R.T.	150	~60	650 → R.T.	150	~60
Heating	R.T. → 650	No O_2 filled	~30	R.T. → 650	150	~30
Annealing	650	150	10/30/60	650	150	10/30/60
Cooling	650 → R.T.	150	~60	650 → R.T.	150	~60

Table 4.2: Annealing procedures for *ex situ* post annealing processes.

Figure 4.6.1 shows the resistance against temperature curves of LSMO films annealed at 150 mTorr for different times. All the films, after going through the usual deposition procedures, were heated up from room temperature in the absence of oxygen until the temperature reached 650 °C (method 3). T_C of the films treated in this way dropped from 340 K to 275 K, as the annealing time increased from 10 to 30 minutes.

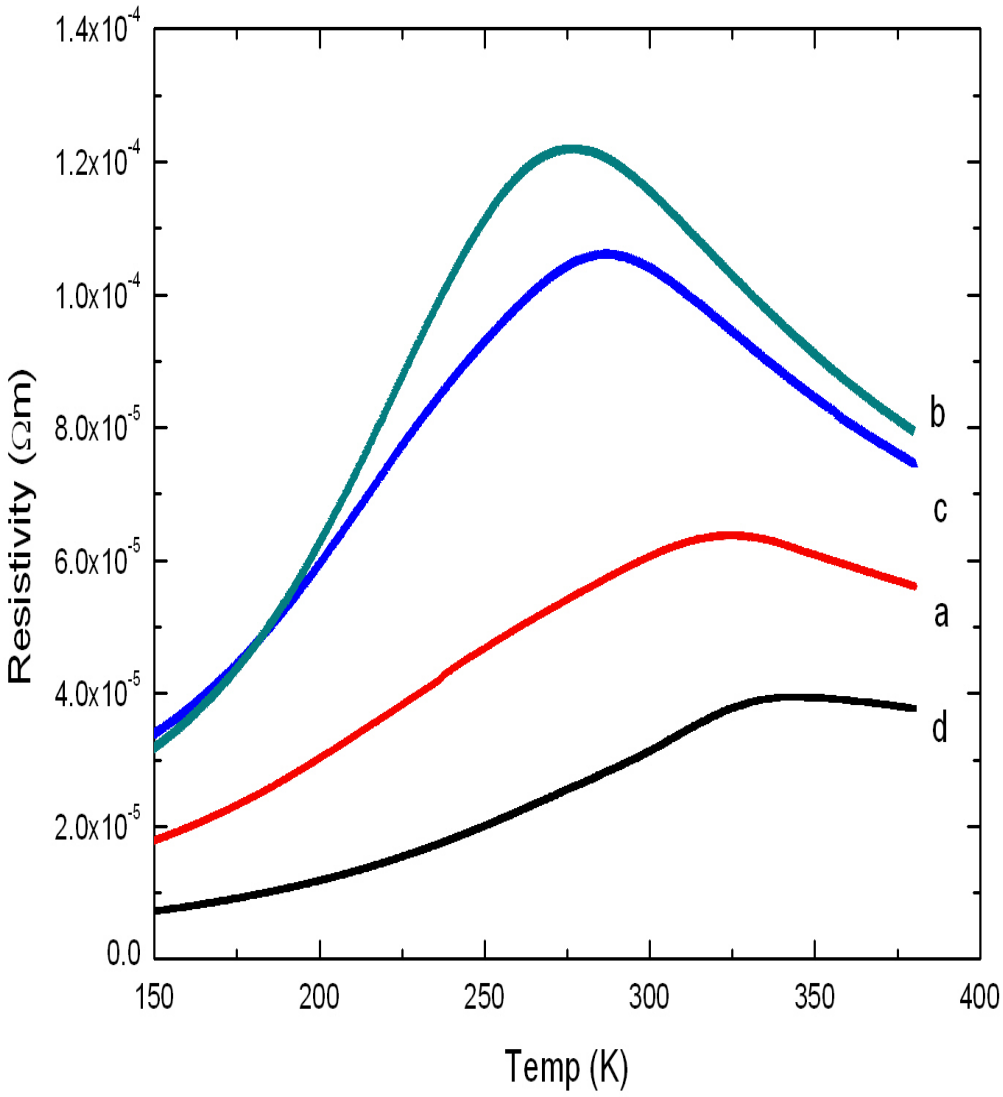

Fig. 4.6.1 Resistance against temperature curves of the films prepared by method 3 in Table 4.2, with different annealing times: (a) 10 minutes (b) 30 minutes (c) 60 minutes (d) without post annealing (cooling under 150 mTorr of oxygen after deposition)

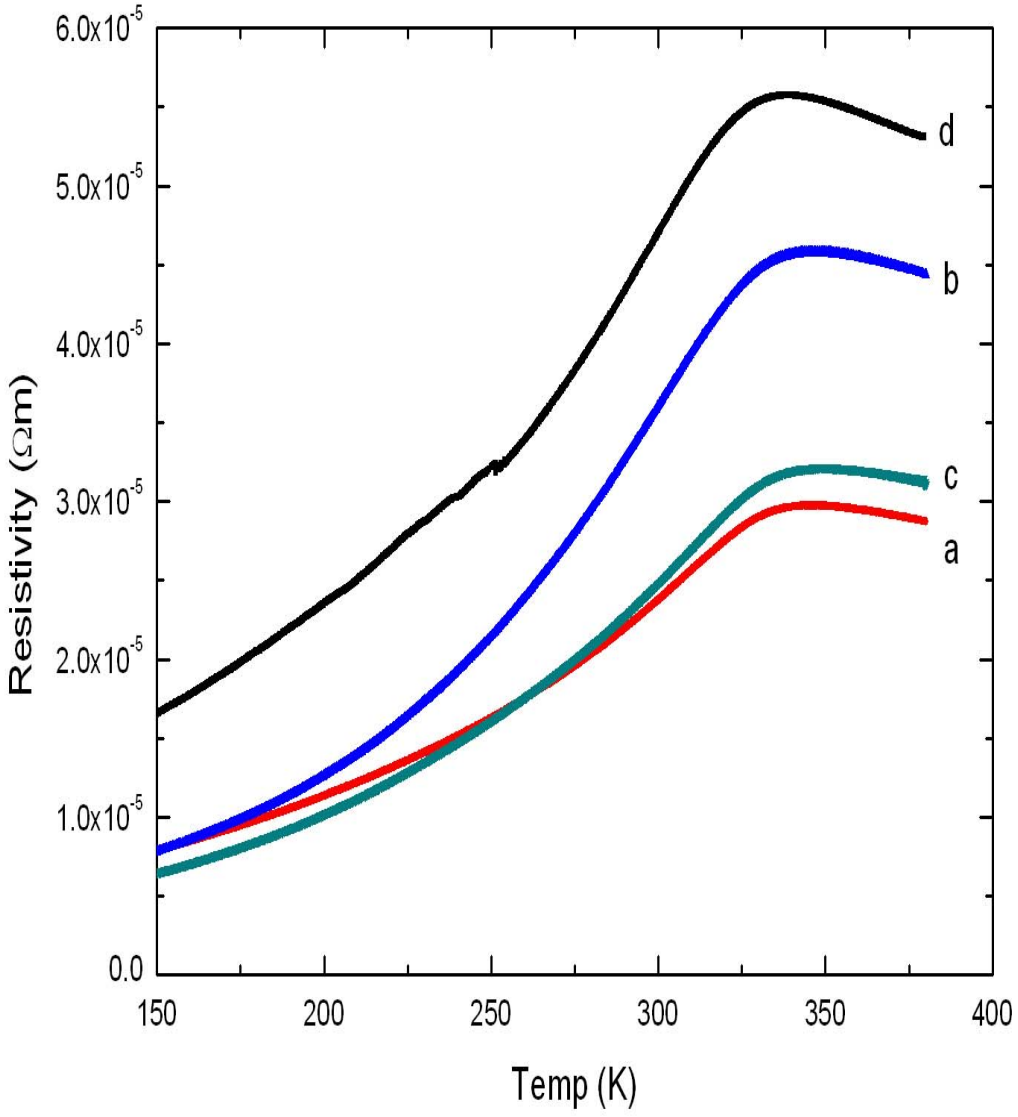

Fig. 4.6.2 Resistance against temperature curves of the films prepared by method 4 in Table 4.2, with different annealing times: (a) 10 minutes (b) 30 minutes (c) 60 minutes (d) without post annealing (cooling under 150 mTorr of oxygen after deposition).

Figure 4.6.2 shows the *R-T* curves of LSMO films annealed at 150 mTorr. The chamber was filled with oxygen when heating started at room temperature (method 4), and we observed that all the curves peaked about 340 K.

By comparing these two figures, we can observe that T_C of the films depends heavily on the correct sequences of post annealing steps. If oxygen was absent from the chamber during the heating stage before annealing, the films would be oxygen deficient. This caused the T_C of the films to drop significantly, which was shown clearly in Fig. 4.6.1.

Great care therefore has to be taken, during either the deposition or the annealing processes, to ensure that the film properties are not altered by subsequent processing steps. For example, if two perovskite layers are deposited and a mechanical mask has to be inserted before depositing the second layer, method 4 should be used if a high T_C of the film is desired.

4.7 Summary

Single-phased (100) LSMO films were grown on single crystal (100) LAO substrates epitaxially, and I have investigated the effect of post annealing procedures on

the properties of LSMO films. We found that the stability of oxide films were highly dependent on the oxygen environment during the annealing procedures. This part of work thus provides useful information for the growth of epitaxial oxide multilayers.

CHAPTER 5

Manganite\Metal Spin Valves

5.1 Introduction

LSMO is one of the ferromagnetic oxides being actively researched in the field of spintronics due to its high spin polarization [38], relatively high *Tc* (Park *et. al*., 1998) and chemical stability. It has been used for GMR junctions [44] and TMR junctions [45]. In both types of junctions, spacers (conductors in GMR junctions, insulators in TMR junctions) are required to perform certain functions as discussed below.

As mentioned in Chapter 2, the spacer in a spin valve structure is used for decoupling two ferromagnetic layers, in order to obtain parallel and anti-parallel magnetization states. On the other hand, for GMR to be observed, spin orientation of the charge carriers must be conserved as they travel through the spacer layer. The thickness of the spacer must be comparable with the electronic mean free path for CIP-GMR, or the spin diffusion lengths for CPP-GMR [17]. Thus, the thickness of the spacer is a crucial parameter affecting the performance of GMR multilayers.

However, there are a few studies on GMR or TMR junctions which do not have

any spacer layers deposited. Ruotolo *et al.* [46] have experimentally demonstrated that LSMO\$Ni_{80}Fe_{20}$ bilayers could exhibit GMR effect. They claimed that the dead layer of LSMO\$Ni_{80}Fe_{20}$ interface can be treated as an intrinsic spacer, with its thickness large enough to suppress magnetic coupling between the bulk of LSMO and NiFe layers. Singh *et al.* [47] reported that magnetite (Fe_3O_4) - manganite (LSMO) bilayers also exhibited GMR at low temperatures. They claimed that a structurally disordered interface was formed at the LSMO\$Fe_3O_4$ interface due to the 6.7 % lattice mismatch between the two materials. As the ferromagnetic coupling mechanism in LSMO is double exchange coupling between Mn^{3+} and Mn^{4+} ions [25], the disordered interface could destroy any double exchange coupling. This will weaken the magnetic coupling between the two magnetic layers.

The above reports concluded that artificial spacer layers are not strictly necessary for GMR devices. In this chapter, I report a study on the magneto-transport properties of LSMO\$Co_{33}Fe_{67}$ spacerless spin valve structure.

5.2 Fabrication of $LaNiO_3$ and $LaNiO_3$\LSMO thin films

In CPP resistance measurements, van de Veerdonk *et al.* [48] reported that inhomogeneous current flow in magnetoresistive junctions could induce a large apparent MR, if the junction resistance was not much larger than the electrode resistance. It is therefore important to construct CPP GMR junctions with a large resistance contrast between the junctions and the electrodes.

In this regard, $LaNiO_3$ (LNO) is a good candidate for electrode material. It has a perovskite pseudo-cubic structure similar to LSMO. Its bulk lattice parameter is a = 3.84 Å. The lattice mismatch between LNO and LAO is -1.3 %. Single-crystal LAO substrates were therefore used in this work in order to obtain epitaxial growth of LNO films. In fact, Zhu *et al*. have shown that LNO films could be epitaxially grown on LAO (100) substrate with strong (100) orientation [49]. The films had metallic behaviour and low resistivity ($\rho = 3\times10^{-6}\,\Omega$m), which is one order of magnitude less than LSMO, $\rho = 5\times10^{-5}\,\Omega$m) [49, 50] and the surfaces can be grown with high smoothness (refer to Section 5.4 and 5.5). These conditions favoured the use of LNO as bottom electrode.

LNO thin films were deposited on LAO (100) substrates at 650 °C by PLD method. The deposition parameters are shown in Appendix B. LNO thin films of thickness

~100 nm were deposited to test their suitability as bottom electrode layers.

For LNO\LSMO samples, LNO was first deposited on LAO (100) substrates with the same procedures described above. Afterwards, the films were cooled down to room temperature naturally at a 150-mTorr oxygen environment. The LNO ablation target was then replaced by LSMO target, before the samples were heated up again to 650 °C under an oxygen pressure of 150 mTorr and annealed for 15 minutes. LSMO films were deposited according to the deposition parameters shown in Appendix A. The deposition time for the LSMO layer was 5 minutes and the thickness was ~50 nm (refer to Section 4.3). Finally, the bilayers were cooled down to room temperature naturally under an oxygen pressure of 150 mTorr.

5.3 Structural characterization of LNO and LNO\LSMO thin films

Structural properties of LNO and LNO\LSMO films were studied by XRD. Figure 5.3.1 shows the θ-2θ scans of a 100-nm thick LNO film grown on LAO (100) substrate. LNO (200) reflection peak was observed at 46.94°, and the out-of-plane lattice constant was estimated to be 3.87Å. Since the lattice constant of bulk LNO was 3.84 Å, the LSMO film was under in-plane compressive stress. The FWHM of the LNO

film was 0.91°, indicating good crystallinity of the film. Figure 5.3.2 shows the ϕ-scans of LNO (202) and LAO (202) planes. The profiles show four reflection peaks of (202) family separated by 90°, indicating both the film and substrate had cubic structures. ϕ angles of the reflection peaks for the film and substrate coincided with each another. It indicates that the LNO film was cube-on-cube grown on the LAO substrate.

Fig. 5.3.3 shows the θ-2θ scan of a LNO\LSMO film sample grown on LAO (100) substrate. By comparing the XRD profiles between a single LNO layer (Fig. 5.3.1) and the LNO\LSMO sample, no additional reflection peaks could be observed. Since the lattice constant of bulk LSMO (3.87 Å) is close to that of bulk LNO (3.84 Å), it is believed that the reflection peaks of LSMO (200) and LNO (200) coincide with each other in the θ-2θ scan. As the XRD scan shows only the peaks of (h00) families of LNO, LSMO and LAO, this means both the LNO and LSMO layers were single-phased and highly textured. Fig. 5.3.4 shows the ϕ scans of LNO (202), LSMO (202) and LAO (202). The four-folded symmetry, and the complete matching of ϕ angles for the reflection peaks of the film and the substrate, shows that LNO and LSMO layers were cube-on-cube grown on the LAO substrate.

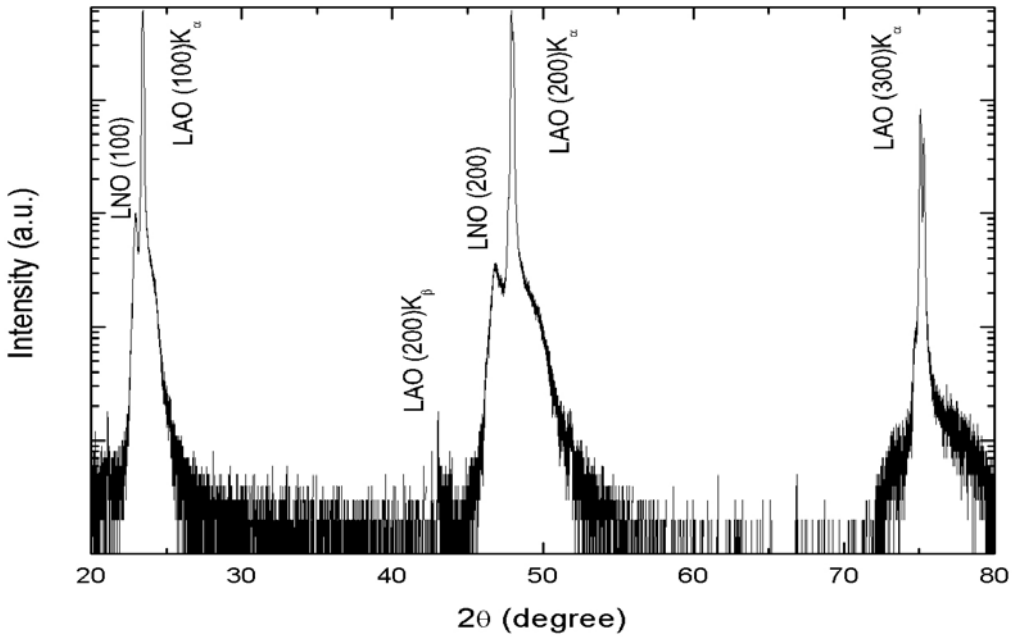

Fig. 5.3.1 XRD *θ-2θ* diffraction pattern of LNO thin film on LAO (100) substrate.

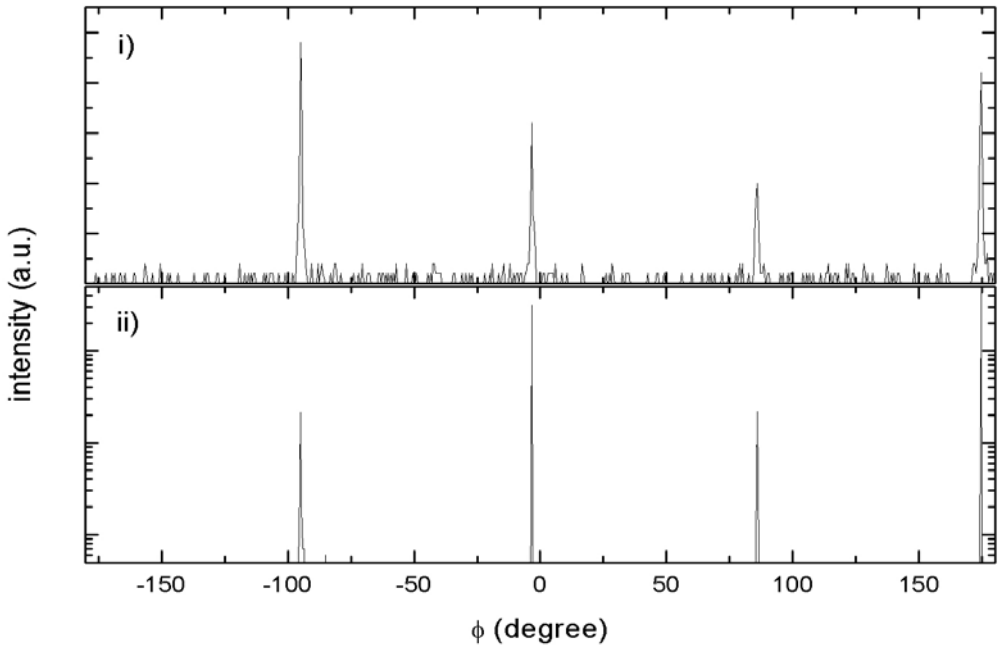

Fig. 5.3.2 *ϕ*-scan of i) LNO (202) and ii) LAO (202), for the same sample as in Fig. 5.3.1.

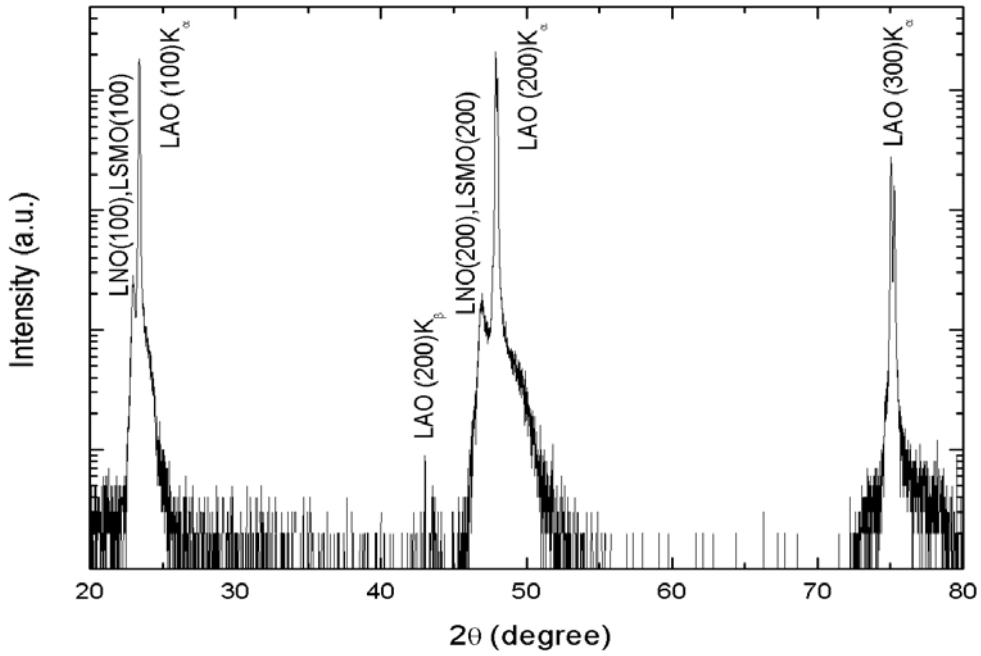

Fig. 5.3.3 XRD θ-2θ diffraction pattern of LNO\LSMO deposited on LAO (100) substrate.

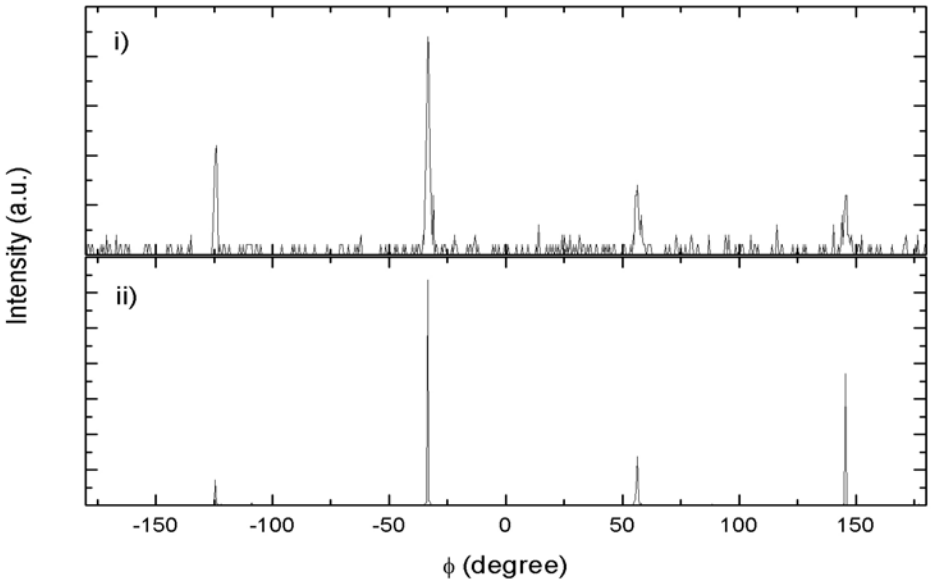

Fig. 5.3.4 ϕ-scan of i) LSMO (202), LNO (202) and ii) LAO (202), for the same sample as in Fig. 5.3.3.

5.4 Surface morphology of LNO and LNO\LSMO thin films

The surface morphologies of LNO and LNO\LSMO films were investigated by AFM. Fig. 5.4.1 shows the AFM images of a LNO film (Fig. 5.4.1 (i)) and a LNO\LSMO sample (Fig. 5.4.1 (ii)). The r.m.s. roughness of LNO and LNO\LSMO samples were about 0.4 nm and 3.1 nm, respectively. The results indicated that smooth and continuous LNO thin films can be grown on LAO. However, the roughness increased as LSMO was deposited on top of LNO. It may be due to the in-plane lattice mismatch between LNO and LSMO [49].

(i)

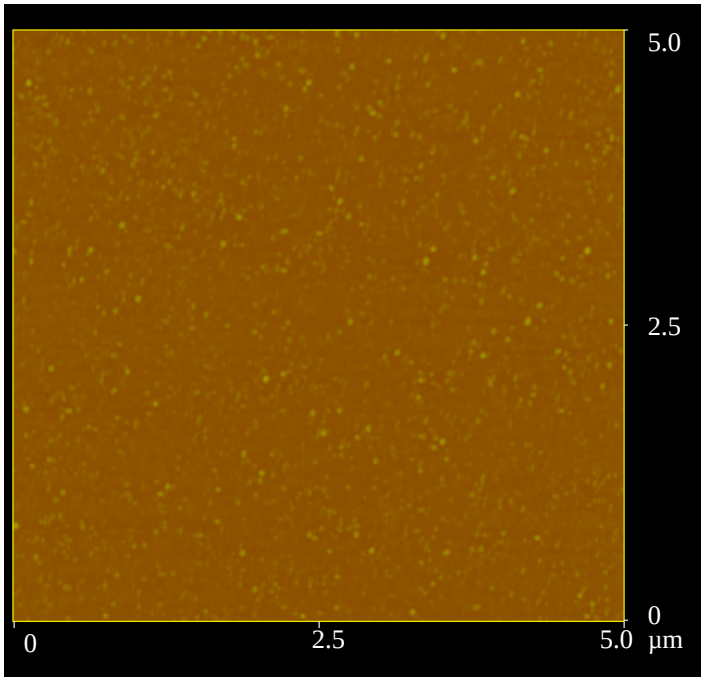

(ii)

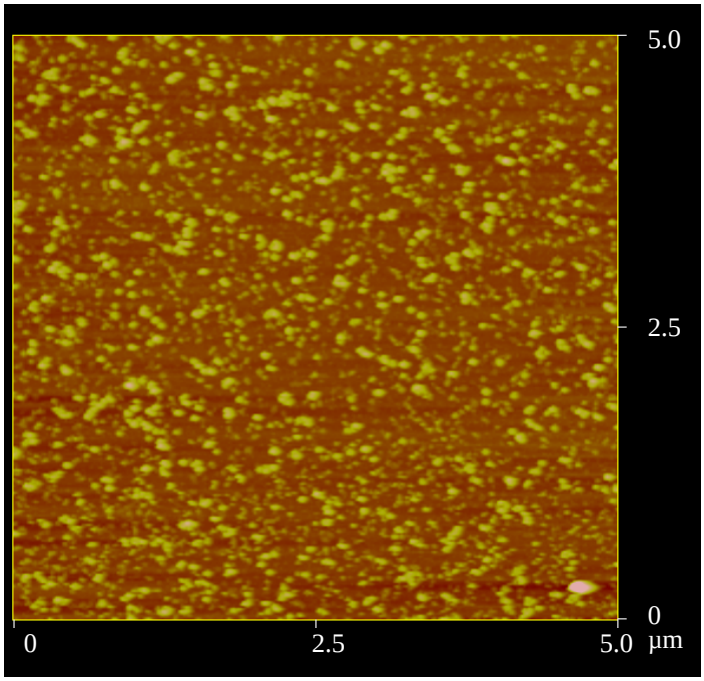

Fig. 5.4.1 AFM images of (i) LNO and (ii) LNO\LSMO thin films.

5.5 Electrical characterization of LNO thin films

Electrical resistances of the films were measured in the temperature range between 20 K and 380 K. Four rectangular-shaped platinum electrodes were deposited on the films by PLD through a mechanical mask. Figure 5.5.1 shows the R-T curve of LNO film, which displays a metallic-like transport behaviour ($\frac{d\rho}{dT}$ >0 for all T). By comparing the R-T curves of LNO and LSMO (Section 4.4), the resistivity of LNO was found to be one order of magnitude less than that of LSMO for the whole temperature range measured.

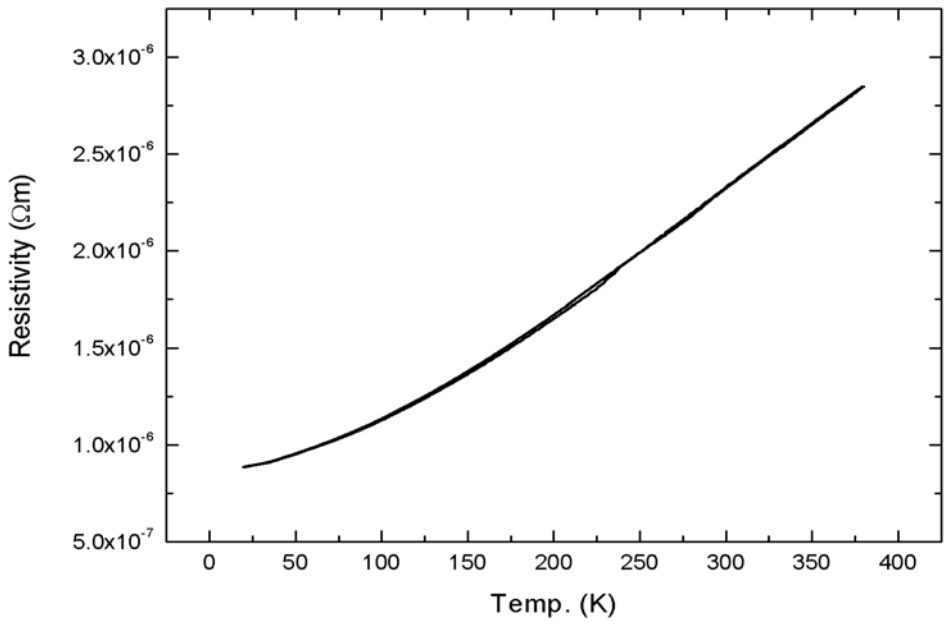

Fig. 5.5.1 Resistivity against temperature of LNO film on LAO (100) substrate.

5.6 Fabrication of LNO\LSMO\$Co_{33}Fe_{67}$ trilayer films

Spin valve samples with LNO, LSMO and $Co_{33}Fe_{67}$ layers were deposited. Firstly, LNO\LSMO were deposited on LAO (100) substrates with the same procedures as described in Section 5.2. Then, a $Co_{33}Fe_{67}$ layer was deposited on the oxide film at room temperature without ambient gas filled, after replacement of the ablation target. The deposition parameters in Appendix C were used for $Co_{33}Fe_{67}$ deposition. The deposition time for $Co_{33}Fe_{67}$ layer was 10 minutes, and the thickness of the layer was ~ 50 nm.

5.7 Structural characterization of LNO\LSMO\$Co_{33}Fe_{67}$ films

XRD measurements were performed on a LNO/LSMO/$Co_{33}Fe_{67}$ trilayer sample. No $Co_{33}Fe_{67}$ characteristic peak was found from the θ-2θ scan profile (Fig 5.7.1). It could be due to the small thickness of the $Co_{33}Fe_{67}$ layer, in combination with the fact that the film deposited at room temperature was polycrystalline.

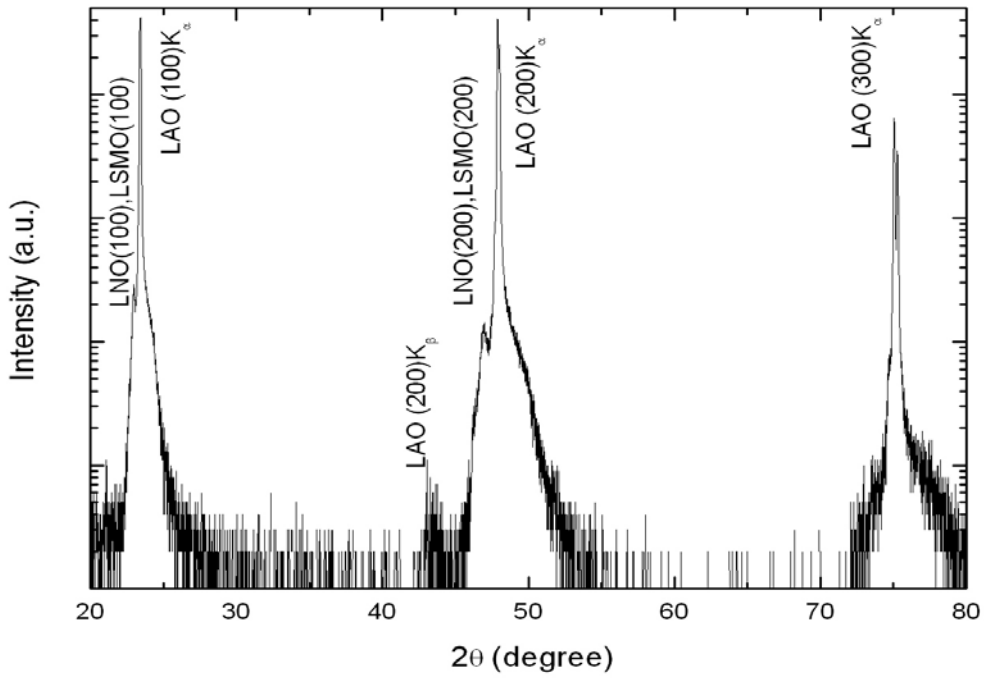

Fig. 5.7.1 XRD *θ-2θ* diffraction pattern of LSMO\LNO\$Co_{33}Fe_{67}$ deposited on LAO (100) substrate.

A trilayer sample with identical structure but deposited on STO substrate was used for TEM investigation. As mentioned previously (Section 4.3), the similar lattice parameters of STO and LAO (substrates) with LNO and LSMO (film materials) ensured that epitaxial films could be obtained generally with either types of substrates. In this TEM study, cross sectional images and diffraction patterns of the sample were obtained. Fig. 5.7.2(i) shows the selected area electron diffraction pattern of the trilayer, performed over a region including all of the layers and the substrate. The image shows a

clear ring which indicates the polycrystalline nature of $Co_{33}Fe_{67}$. And the spots indicate that the LSMO and LNO films were epitixially grown on the substrate.

Fig. 5.7.2(ii) shows the image of the cross section of the trilayer sample. A narrow, white strip at the boundary between LSMO and $Co_{33}Fe_{67}$ could be observed, suggesting a different crystallographic structure in that region. However, the exact nature of this region could not be studied from the figure due to limited spatial resolution of the image. Fix *et al.* [51] have fabricated Sr_2FeMoO_6\$SrTiO_3$\$CoFe_2$ tunneling junctions by PLD on STO (100) substrate and investigated the nature of interfaces by TEM and electron energy loss spectroscopy (EELS) techniques. They have obtained a sharp interface between STO/$CoFe_2$. Their EELS results indicated very low oxygen concentration in the $CoFe_2$ layer when it was deposited at low temperature (50 °C). It indicates that the oxidization of $CoFe_2$ was not significant in their samples. I believe that a similar situation has also happened in the LSMO\$Co_{33}Fe_{67}$ interface for the sample in Fig. 5.7.2, as the metallic layer was deposited at room temperature. Further investigations, however, is necessary to provide direct evidence on this suggestion.

(i)

(ii)

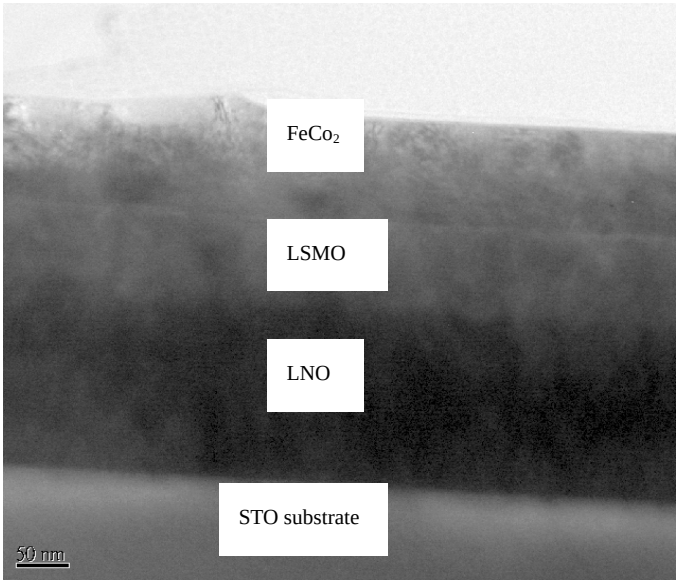

Fig. 5.7.2 TEM images of LNO\LSMO\$Co_{33}Fe_{67}$ on STO substrate (i) selected area diffraction pattern and (ii) cross section image.

5.8 Magnetic characterization of LNO\LSMO\$Co_{33}Fe_{67}$

VSM was used to study the magnetic properties of the samples. Hysteresis (M(H)) loops were measured at 100 K with the magnetic field applied parallel to the film plane along the substrate's [001] axis. Fig. 5.8.1 shows M(H) loops of $Co_{33}Fe_{67}$ (i) and LNO\LSMO (ii). The coercivity values of $Co_{33}Fe_{67}$ and LSMO were 20 Oe and 105 Oe respectively. The difference of coercivity values was large enough to obtain well-defined parallel and anti-parallel configurations in the pseudo spin valve samples.

Fig. 5.8.2(i) shows the M(H) loop of LNO\LSMO\$Co_{33}Fe_{67}$ at 100 K. It clearly shows two distinct coercive fields at 20 Oe and 100 Oe, corresponding to the $Co_{33}Fe_{67}$ and LSMO layers, respectively. In Section 5.7, we mentioned that an interface region was observed between LSMO and $Co_{33}Fe_{67}$. This suggests that the interface region acted as a spacer, which decoupled the LSMO and $Co_{33}Fe_{67}$ layers effectively.

Fig. 5.8.2(ii) shows the M(H) loop measured at 10 K and 50 K. By comparing with Fig. 5.8.2(i), it reveals that the coercivity of both LSMO and $Co_{33}Fe_{67}$ were increased. Also, well-established parallel and anti-parallel configurations of M(H) loop were still obtained.

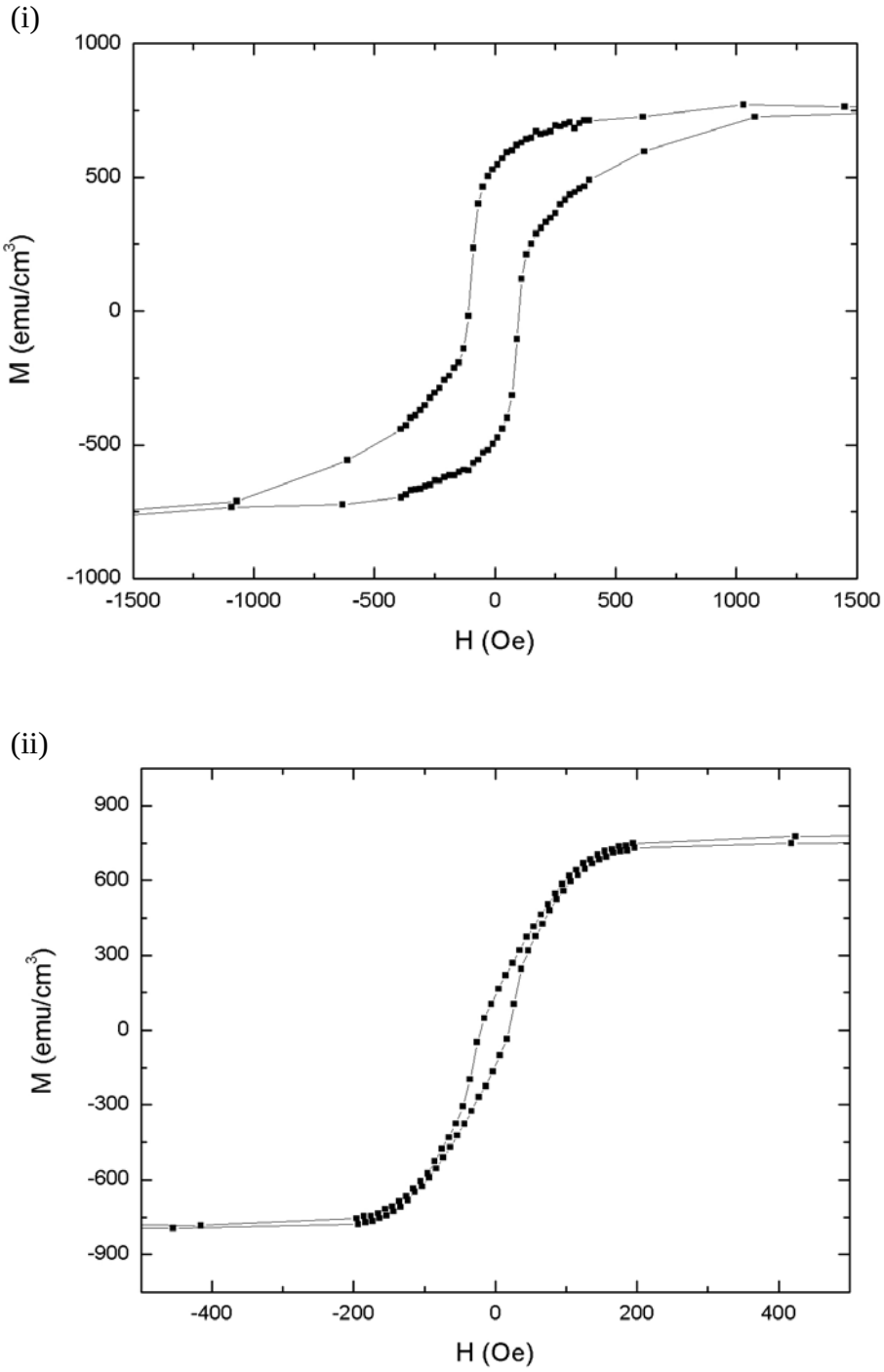

Fig. 5.8.1 M(H) loop of (i) LNO\LSMO and (ii) $Co_{33}Fe_{67}$ single layer at 100 K.

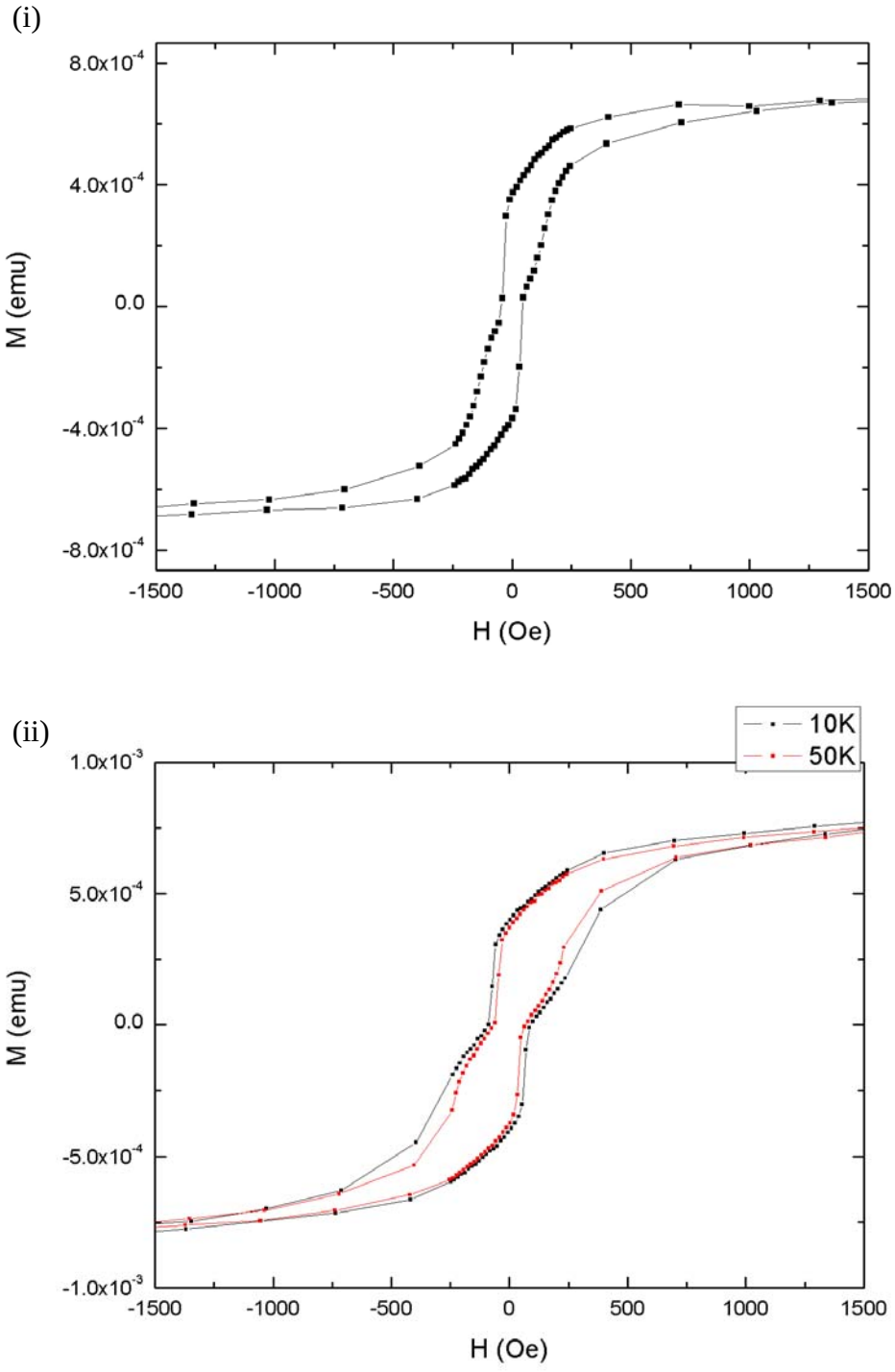

Fig. 5.8.2 M(H) loops of LNO\LSMO\$Co_{33}Fe_{67}$ at (i) 100 K and (ii) 10 K and 50 K.

5.9 Magneto-transport characterization of LNO\LSMO

In Chapter 2, I introduced different types of MR. In this work, I aimed at investigating the GMR effect of CPP pseudo spin valve structure. However, other types of MR, such as AMR from the $Co_{33}Fe_{67}$ and LSMO layers, can contribute to the observed MR. While the AMR effect is small for $Co_{33}Fe_{67}$ (less than 0.2 %) [5], it can be substantial in polycrystalline LSMO films (up to 15 % at a field of 1500 Oe) [52]. Such a MR ratio can be comparable with that of the GMR effect. Therefore, the AMR effect of LSMO films has to be checked.

To study the magneto-transport properties of LSMO, LNO\LSMO\Pt junctions were fabricated (Fig. 5.9.1(i)). LNO films were deposited on LAO substrates as bottom electrodes. Then LSMO layers were deposited through a thin stainless steel shadow mask with 200 μm squares. Finally, Pt electrodes were deposited on top of LSMO, by using the same shadow mask.

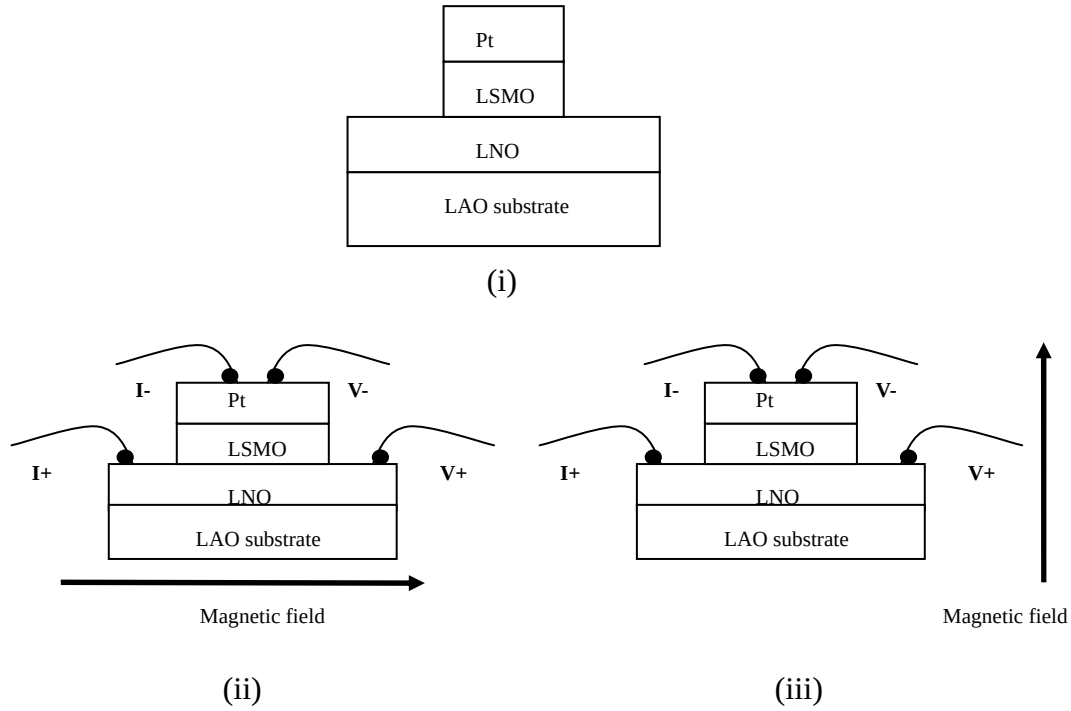

Fig. 5.9.1(i) Schematic diagram of a LNO\LSMO\Pt junction. Configurations for magneto-transport measurements: (ii) current perpendicular to magnetic field across the junction, (iii) current parallel to magnetic field across the junction.

Fig. 5.9.2 shows the MR measured with magnetic field applied parallel or perpendicular to the junctions (Fig. 5.9.1(ii) and (iii)) at 20 K. Here, the MR is defined as

$$\frac{R(H)-R(Hc)}{R(Hc)} \qquad (5.9.1)$$

where H_c is the coercivity. The maximum magnitude of MR obtained was smaller than 0.1 % (within the field range of ±1 kOe) in both configurations. However, the graph of

MR against magnetic field (MR(*H*)) indicates that both measurements have shown negative MR behaviour. As mentioned in Chapter 2, the sign of MR depends on the applied current and magnetic field directions for AMR effect. That means the AMR effect was not significant. One of possible reasons for the observation was due to the spin-dependent scattering of polarized electrons at the grain boundaries, which is a manifestation of the GMR effect [52].

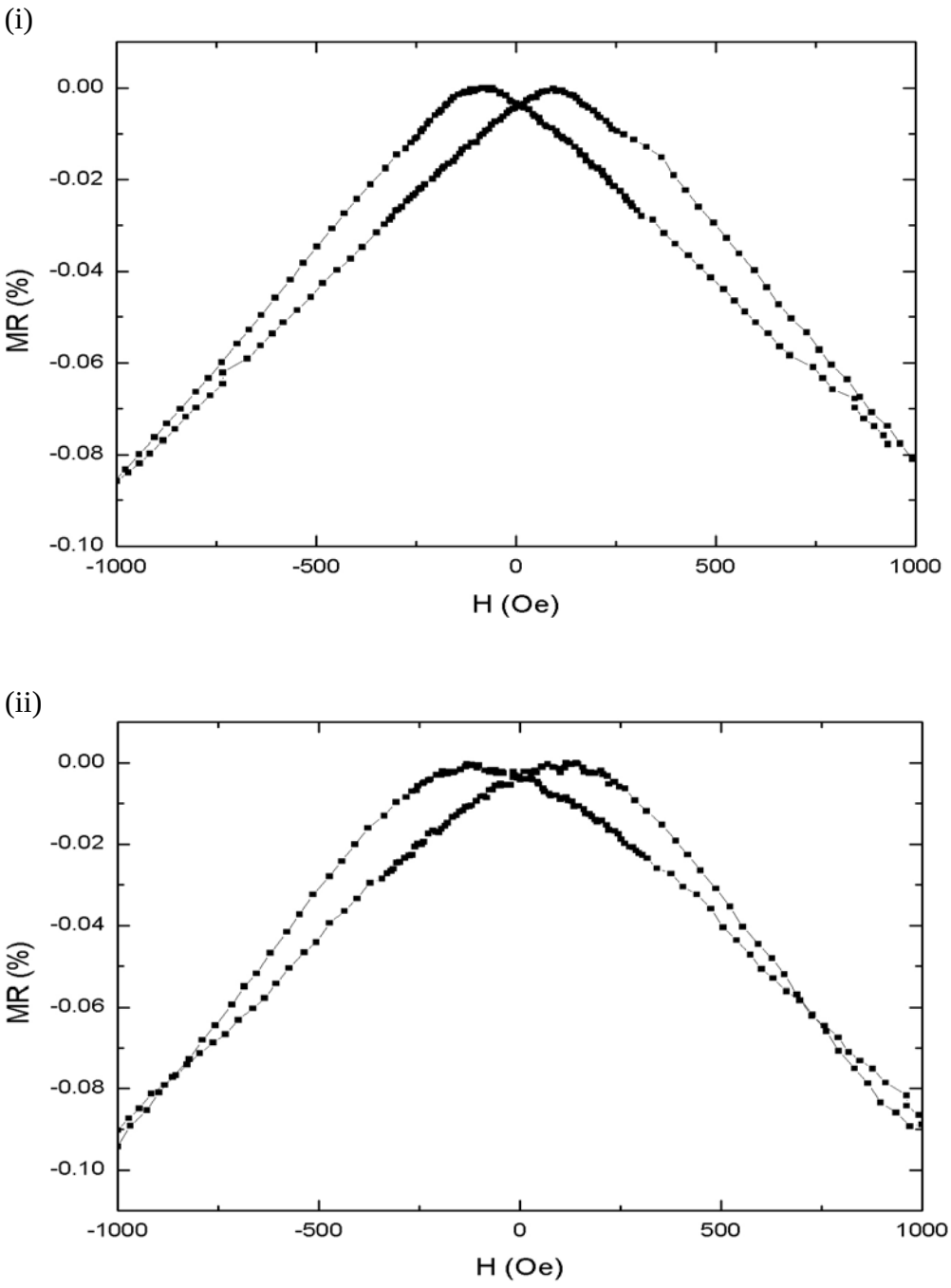

Fig. 5.9.2 MR(H) of LSMO with (i) H applied parallel to the current, and (ii) H applied perpendicular to the current at 20K.

5.10 Magneto-transport properties of LNO\LSMO\$Co_{33}Fe_{67}$

LNO\LSMO\$Co_{33}Fe_{67}$ junctions were fabricated for magneto-transport measurements. Firstly, LNO films were deposited on LAO substrates as bottom electrodes. Then LSMO squares (200 μm in size) were deposited on top of LNO through a thin stainless steel shadow mask. Finally, $Co_{33}Fe_{67}$ layer was deposited on top of the LSMO layer by using the same shadow mask. The final structure is shown in Fig. 5.10.1.

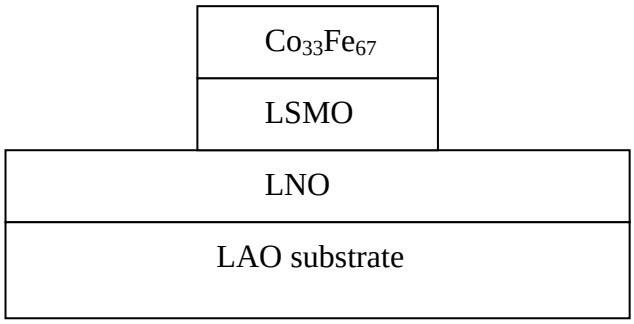

Fig. 5.10.1 Schematic diagram of LNO\LSMO\$Co_{33}Fe_{67}$ junction.

The CPP MR of the junction was measured at various temperatures. With a magnetic field applied parallel to the film plane, the resistances of the junctions were obtained by applying a constant current of 10 mA and measuring the corresponding voltage drop (Fig. 5.10.2).

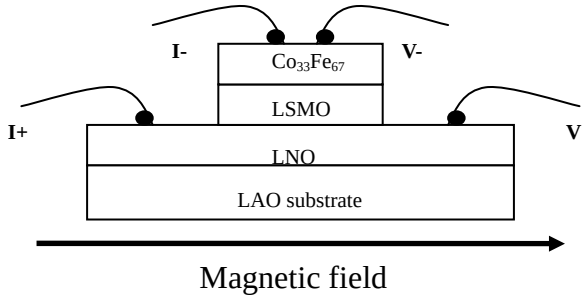

Fig. 5.10.2 Measurement configuration of LNO\LSMO\$Co_{33}Fe_{67}$ junctions.

Fig. 5.10.3 shows the MR(*H*) of a trilayer junction at 10 K and the corresponding MH loop. A high resistance state was observed from the junction, as a 1 kOe in-plane magnetic field was applied (which was sufficient to saturate both of the LSMO and the $Co_{33}Fe_{67}$ layers). When the magnetic field gradually decreased to -20 Oe (coercive field of $Co_{33}Fe_{67}$), the magnetization of $Co_{33}Fe_{67}$ layer changed accordingly. An anti-parallel magnetization configuration was obtained, and MR(*H*) showed a low resistance state (between the coercive field of LSMO and $Co_{33}Fe_{67}$). As the magnetic field was further decreased, the magnetization of LSMO was switched. Parallel magnetization configuration was obtained, and the junction switched back to the high resistance state. The whole process was repeated as the field ramped up from -1 kOe back to 1 kOe.

Fig. 5.10.4 shows the MR(*H*) of the same junction at different temperatures. As the temperature decreased, the MR increased significantly. It may be due to the decrease of electron-phonon scattering which can reduce the overall resistance of the junction (refer

to Fig.5.10.5). Magnon scattering, which can be greatly suppressed at low temperatures (< T_c), can reduce the GMR effect as mentioned in Section 2.2.3. An increase of spin polarization with a decreasing temperature is also a possible reason of the MR enhancement. At 10 K, a MR ratio of 1.65 % was obtained at 500 Oe, which was much greater than that of a single layer of LSMO shown in previous section

From Fig 5.10.3, an inverse GMR behaviour was observed. Vouille *et al*. [17] reported that inverse GMR effect can obtained by using two materials with different signs of spin asymmetries. On the other hand, the sign of MR also depends on the interfacial spin asymmetry [17, 53]. Spin polarization is defined by

$$P = \frac{n_\uparrow - n_\downarrow}{n_\uparrow + n_\downarrow} \qquad (5.9.1)$$

where n_i (i = ↑and ↓) is the density of state of the spin sub-band *i* at Fermi level. As LSMO is a positive spin polarization material, I suggest that the inverse GMR of our junction may be due to the negative spin polarization of either bulk $Co_{33}Fe_{67}$ or LSMO\ $Co_{33}Fe_{67}$ interface

In CPP resistance measurements, van de Veerdonk *et al.* [48] reported that an inhomogeneous current flow could induce a large apparent MR, if the junction resistance was not much larger than the electrode resistance. Calculations by Ruotolo *et*

al. [46] showed that LSMO (ρ = 1.2×10^{-6} Ωm at 4.2 K) junctions of area 100 μm×70 μm, when used as the bottom electrode, could rule out any geometrical MR effect. For my 200-μm square junctions, I used LNO as the bottom electrode of the junction, with resistivity smaller than LSMO. In my junction showed in Fig. 5.10.1, the junction resistance (R_j) includes the resistance of LSMO and LSMO\$Co_{33}Fe_{67}$ interface. As the resistance of LSMO was R_{LSMO} = 66 Ω/sq and LNO electrode was R_{LNO} = 8.9 Ω/sq, corresponding to resistivity ρ_{LSMO} =3.3×10^{-6} Ωm and ρ_{LNO} =8.9×10^{-7} Ωm measured at 20 K. The ratio R_{LSMO}/R_{LNO} was 7.4. Thus, the ratio of R_j/R_{lead} was much larger than that value. According to van de Veerdonk *et al.* [48], the ratio was large enough that the geometrical effect could be neglected.

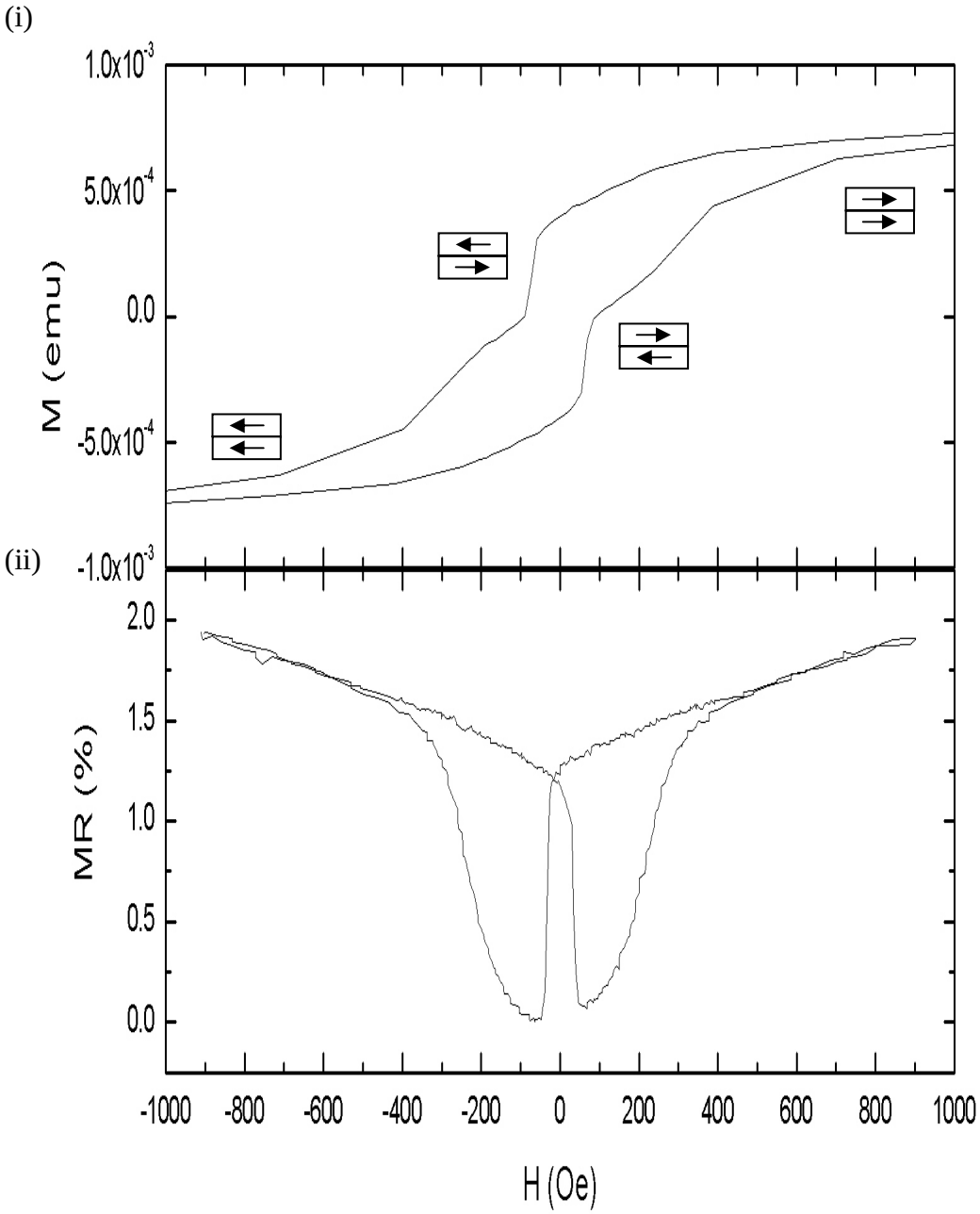

Fig. 5.10.3 MH loop (i) and MR(H) (ii) of a LNO\LSMO\$Co_{33}Fe_{67}$ junction at 10 K.

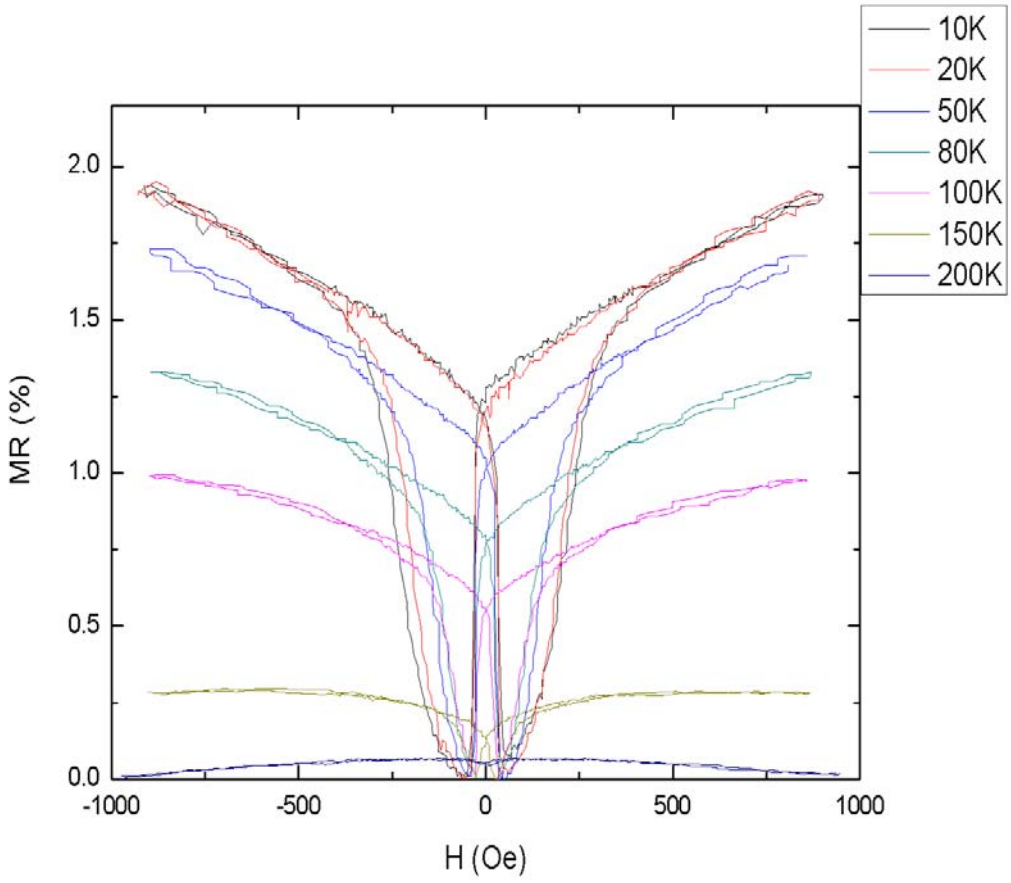

Fig. 5.10.4 MR(H) of a LNO\LSMO\$Co_{33}Fe_{67}$ junction at different temperatures.

To confirm that the observed magnetoresistive effects were not contributed from TMR effect, I performed IV measurement at different temperatures for the junction. Fig. 5.10.5(i) shows the IV characteristics of the LNO\LSMO\$Co_{33}Fe_{67}$ junction at different temperatures. All of the IVs were linear within the range of applied voltages (± 0.05V), which indicated Ohmic CPP transport characteristics. Fig. 5.10.5(ii) plots the resistance of the junction at various temperatures. The resistance of junction increased as the temperature increased. No signs of tunnel transport can be found from the results.

(i)

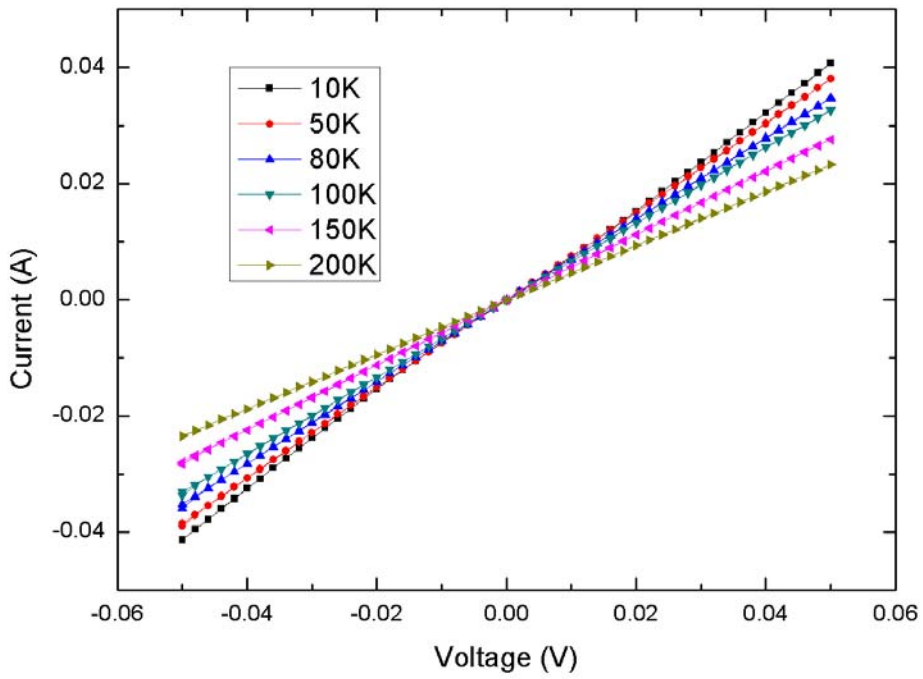

(ii)

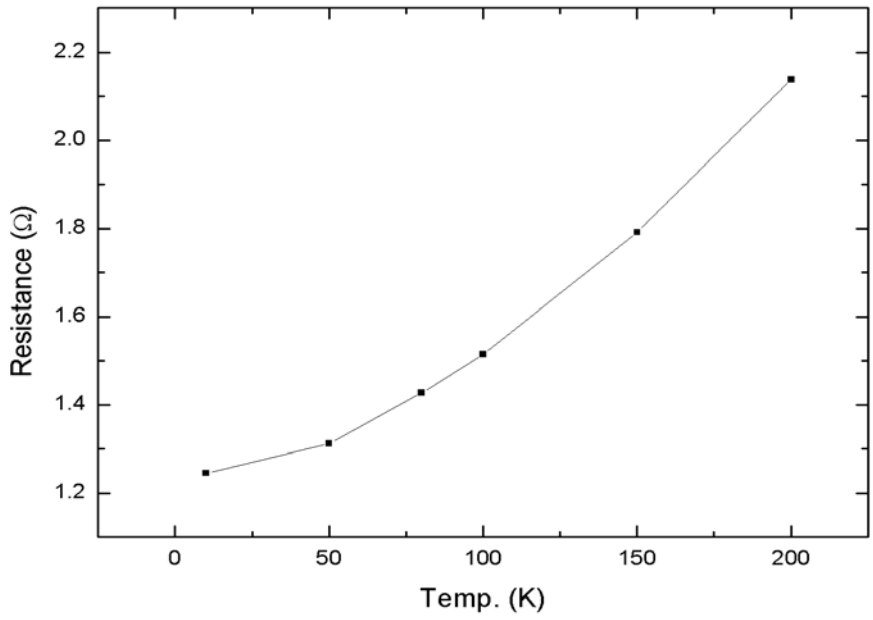

Fig. 5.10.5 (i) IV characteristics at different temperatures and (ii) resistance against temperature of LNO\LSMO\$Co_{33}Fe_{67}$ junction, under a bias voltage of 10mV.

5.11 Summary

It has been shown that single-phased (100) LNO films could be epitaxially grown on (100) LAO single crystal substrates. Also single-phased (100) LSMO films can be cube-on-cube grown on (100) LNO with good crystallinity. I have fabricated LNO\LSMO\$Co_{33}Fe_{67}$ junctions and investigated their magneto-transport behaviour. I demonstrated the possibility of fabricating pseudo spin valves without using an extrinsic spacer. The interface between LSMO and $Co_{33}Fe_{67}$ can be treated as an intrinsic spacer in pseudo spin valve fabrication.

CHAPTER 6

Conclusions

Post annealing of LSMO films

LSMO films have been fabricated on LAO single crystal substrates by PLD. From the XRD measurements, it has been shown that single-phased (100) LSMO films could be epitaxially grown on LAO(100) single crystal substrates with high crystallinity and strong orientations. The peaks of resistance against temperature (R-T) profiles were used to estimate the Curie temperatures of the films. R-T curves of as-grown LSMO films had a transition from metallic-like to semiconducting-like resistance behaviour, similar to results reported in literature.

The estimated Curie temperatures of LSMO films were shown to vary according to deposition conditions, as well as annealing processes. I have investigated the effect of different post annealing on the properties of LSMO films. The results indicated that the stability of oxide films was highly dependent on the oxygen environment, annealing steps and procedures.

LNO\LSMO bilayers

I have fabricated LNO films on LAO single crystal substrates, serving as bottom electrodes for GMR junctions. The XRD results showed that (100) LNO could be epitaxially grown on (100) LAO single crystal substrates. Single-phased (100) LSMO films can be cube-on-cube grown on top of (100) LNO films with good crystallinity. The surface morphology of LNO and LNO\LSMO films were investigated by AFM. The r.m.s. roughness of LNO and LNO\LSMO samples were about 0.4 nm and 3.1 nm, respectively. The results indicated that smooth and continuous LNO thin films can be grown on LAO, and roughness increased as LSMO was deposited on top of LNO.

Electrical resistances of the LNO films were measured in the temperature range between 20 K and 380 K. The R-T curve of LNO film, which displayed metallic-like behaviour, showed resistivity values that was at least one order of magnitude less than that of LSMO films for the whole temperature range measured. Besides, magneto-transport properties of LNO\LSMO bilayers were investigated. MR measurements indicated that AMR was not significant, although GMR effect was present due to spin-dependent scattering of polarized electron at grain boundaries.

LNO\LSMO\$Co_{33}Fe_{67}$ trilayers

I have also fabricated LNO\LSMO\$Co_{33}Fe_{67}$ trilayers and investigated their structural and magnetic properties, and magneto-transport behaviour. XRD could not show characteristic peaks related to $Co_{33}Fe_{67}$. It could be due to the small thickness of $Co_{33}Fe_{67}$, in combination with the fact that films deposited at room temperature were polycrystalline. The latter suggestion was further supported by TEM study of a trilayer sample with identical structure but deposited on STO(100) substrate. Selected area electron diffraction pattern of the trilayer showed a clear ring, which indicated the polycrystalline nature of $Co_{33}Fe_{67}$. An interface region between LSMO and $Co_{33}Fe_{67}$ was observed in the cross sectional TEM image of the trilayer sample.

VSM was used to study the magnetic properties of trilayer samples. The coercivity values of $Co_{33}Fe_{67}$ and LSMO were 20 Oe and 105 Oe respectively. M(H) loop of LNO\LSMO\$Co_{33}Fe_{67}$ at 100 K clearly showed two distinct coercive fields at 20 Oe and 100 Oe, corresponding to the $Co_{33}Fe_{67}$ and LSMO layers, respectively. This suggested that the interface region acted as a spacer, which reduced the coupling between LSMO and $Co_{33}Fe_{67}$ layers.

In magneto transport measurements, the excellent matching of MR(*H*) and MH

loops helped to distinguish the parallel and anti parallel resistance states in the trilayer sample, demonstrating the GMR behaviour. The inverse GMR of the junctions may be due to either bulk $Co_{33}Fe_{67}$ or interface between two ferromagnetic layers with negative spin polarization.

In conclusion, I have successfully demonstrated the fabrication of pseudo spin valves without using extrinsic spacers. The interfaces between magnetic oxides and metals can be treated as intrinsic spacers in pseudo spin valve fabrications. However, the MR shown by the trilayer samples was small and observable only at low temperatures. It may be due to the nature or the thickness of the interface layer. In order to obtain higher MR ratios, more thorough understandings of the interface physics and film growth processes are needed.

Appendix A: $La_{0.7}Sr_{0.3}MnO_3$ PLD parameters

Substrate temperature	650 °C
Laser fluence	3.6 Jcm^{-2}
Laser pulse frequency	5 Hz
Substrate – target distance	4 cm
Chamber base pressure	5 mTorr
Oxygen pressure	150 mTorr
Pre annealing temperature	650 °C
Pre annealing oxygen pressure	150 mTorr
Pre annealing time	10 minutes
Deposition rate	~20 nm/min
Oxygen pressure during cooling	150 mTorr

Table A: Optimal parameters for pulsed laser deposition of $La_{0.7}Sr_{0.3}MnO_{3.}$

Appendix B: $LaNiO_3$ PLD parameters

Substrate temperature	650 °C
Laser fluence	3.6 Jcm^{-2}
Laser pulse frequency	5 Hz
Substrate – target distance	4 cm
Chamber base pressure	5 mTorr
Oxygen pressure	150 mTorr
Pre annealing temperature	650 °C
Pre annealing oxygen pressure	150 mTorr
Pre annealing time	10 minutes
Deposition rate	~5 nm/min
Oxygen pressure during cooling	150 mTorr

Table B: Optimal parameters for pulsed laser deposition of $LaNiO_3$.

Appendix C: $Co_{33}Fe_{67}$ PLD parameters

Substrate temperature	Room Temperature
Laser fluence	3.6 Jcm^{-2}
Laser pulse frequency	10 Hz
Substrate – target distance	4 cm
Chamber pressure	4×10^{-5} mTorr
Deposition rate	~5 nm/min

Table C: Optimal parameters for pulsed laser deposition of $Co_{33}Fe_{67}$.

References

[1] R. J. Soulen, Jr., J. M. Byers, M. S. Osofsky, B. Nadgorny, T. Ambrose, S. F. Cheng, P. R. Broussard, C. T. Tanaka, J. Nowak, J. S. Moodera, A. Barry, and J. M. D. Coey, "Measuring the spin polarization of a metal with a superconducting point contact", Science **282**, 85 (1998).

[2] J. M. Daughton, "GMR applications", J. Magn. Magn. Mater. **192**, 334-342 (1999).

[3] T. R. McGuire and R. I. Potter, "Anisotropic magnetoresistance in ferromagnetic 3d alloys", IEEE Trans. Magn. **11**, 1018-1038 (1975).

[4] M. Julliere, "Tunneling between ferromagnetic films", Phys. Lett. A **54**, 225-226 (1975).

[5] J. S. Moodera, L. R. Kinder, T. M. Wong, and R. Meservey, "Large magnetoresistance at room temperature in ferromagnetic thin film tunnel junctions", Phys. Rev. Lett. **74**, 3273-3276 (1995).

[6] Djayaprawira, D. David, K. Tsunekawa, M. Nagai, H. Maehara, S. Yamagata, N. Watanabe, S. Yuasa, Y. Suzuki and K. Ando, "230% room-temperature

magnetoresistance in CoFeB/MgO/CoFeB magnetic tunnel junctions", Appl. Phys. Lett. **86**, 092502 (2005).

[7] S. Jin, T. H. Tiefel, M. McCormack, R. A. Fastnacht, R. Ramesh, and L. H. Chen, "Thousandfold change in resistivity in magnetoresistive La-Ca-Mn-O Films", Science **264**, 413-415 (1994).

[8] K. I. Kobayashi, T. Kimura, H. Sawada, K. Terakura, and Y. Tokura, "Double perovskites", Nature **395**, 677 (1998).

[9] M. N. Baibich, J. M. Broto, A. Fert, F. N. Van Dau, F. Petroff and P. Eitenne, "Giant magnetoresistance of (001)Fe / (001)Cr magnetic superlattices", Phys. Rev. Lett. **61**, 2472-2475 (1988).

[10] J. Mathon, "Exchange interactions and giant magnetoresistance in magnetic multilayers", Contemporary Physics **32**, 143-156 (1991).

[11] M.M.H. Willekens, T.G.S.M. Rijks, H.J.M. Swagten and W.J.M. deJonge, "Interface intermixing and magnetoresistance in Co/Cu spin valves with uncoupled Co layers", J. Appl. Phys. **78**, 7202-7209 (1995).

[12] A. Ruotolo, "Focused ion beam patterning and imaging of novel spintronic devices for digital magnetic data storage, magnetic field sensing and quantum computing", PhD Thesis, University of Naples, (2006).

[13] J. Mathon, "Ab initio calculation of the perpendicular giant magnetoresistance of finite Co/Cu(001) and Fe/Cr(001) superlattices with fluctuating layer thicknesses", Phys. Rev. B **55**, 960-969 (1997).

[14] S.S.P. Parkin, "Systematic variation of the strength and oscillation period of indirect magnetic exchange coupling through the 3*d*, 4*d*, and 5*d* transition metals", Phys. Rev. Lett. **67**, 3598 (1991)

[15] N. F. Mott, "Electrons in transition metals", Advances in Physics **13**, 325 (1964).

[16] J. F. Gregg, I. Petej, E. Jouguelet and C. Dennis, "Spin electronics" , J. Phys. D: Appl. Phys. **35**, R121-R155 (2002).

[17] A. Vouille, A. Barthelemy, F. Elokan Mpondo, A. Fert, P. A. Schroeder, S. Y. Hsu, A. Reilly and R. Loloee, "Microscopic mechanisms of giant magnetoresistance", Phys. Rev. B **60**, 6710-6722 (1999).

[18] B. Dieny, V. S. Speriosu, S. S. P. Parkin, B. A. Gurney, D. R. Wilhoit and D. Mauri, "Giant magnetoresistive in soft ferromagnetic multilayers", Phys. Rev. B **43**, 1297-1300 (1991).

[19] J. Nogués, and I. K. Schuller, "Exchange bias", J. Magn. Magn. Mater. **192**, 203-232 (1999).

[20] W. S. Lew, A. Samad, S. P. Li, L. Lopez-Diaz, G. X. Cheng and J. A. C. Bland, "Magnetic properties of epitaxial NiFe/Cu/Co spin-valve structures on GaAs(001)", J. Appl. Phys. **87**, 5947-5949 (2000).

[21] W. Zou, H. N. G. Wadley, X. W. Zhou and R. A. Johnson, "Surfactant-mediated growth of giant magnetoresistance multilayers", Phys. Rev. B **64**, 174418 (2001).

[22] G. H. Jonker and J. H. Van Santen, "Ferromagnetic compounds of manganese with perovskite structure", Physica **16**, 337-349 (1950).

[23] J. H. Van Santen and G. H. Jonker, "Electrical conductivity of ferromagnetic compounds of manganese with perovskite structure", Physica **16**, 599-600 (1950).

[24] R. Von Helmolt, J. Wecker, B. Holzapfel, L. Schultz and K. Samwer, "Giant

negative magnetoresistance in perovskitelike $La_{2/3}Ba_{1/3}MnO_x$ ferromagnetic films", Phys. Rev. Lett. **71**, 2331-2333 (1993).

[25] Haghiri-Gosnet and J. Renard, "CMR manganites: physics, thin films and devices", J. Phys. D: Appl. Phys. **36**, R127-R150 (2003).

[26] J. Fontcuberta, B. Martinez, A. Seffar, S. Pinol, J. L. Garcia-Munoz and X. Obradors, "Colossal magnetoresistance of ferromagnetic manganites: structural tuning and mechanisms", Phys. Rev. Lett. **76**, 1122-1125 (1996).

[27] P. Dai, J. Zhang, H. A. Mook, S. Liou, P. A. Dowben and E. W. Plummer, "Experimental evidence for the dynamic Jahn-Teller effect in $La_{0.65}Ca_{0.35}MnO_3$", Phys. Rev. B **54**, R3694-R3697 (1996).

[28] A. Zener, "Interaction between the *d*-shells in the transition metals. II. Ferromagnetic compounds of manganese with perovskite structure", Phys. Rev. **82**, 403-405 (1951).

[29] P. W. Anderson and H. Hasegawa, "Considerations on double exchange", Phys. Rev. **100**, 675-681 (1955).

[30] R. A. De Groot, F. M. Mueller, P. G.. Engen and K. H. J. Buschow, "New class of materials: half-metallic ferromagnets", Phys. Rev. Lett. **50**, 2024-2027 (1983).

[31] D. Dijkkamp, T. Venkatesan, X. D. Wu, S. A. Shaheen, N. Jisrawi, Y. H. Min-Lee, "Preparation of Y-Ba-Cu oxide superconductor thin films using pulsed laser evaporation from high T_c bulk material", Appl. Phys. Lett. **51**, 619-621 (1987).

[32] R. Ramesh, K. Luther, B. Wilkens, D. L. Hart, E. Wang, J. M. Tarascon, "Epitaxial growth of ferroelectric bismuth titanate thin films by pulsed laser deposition", Appl. Phys. Lett. **57**, 1505-1507 (1990).

[33] R. Von Helmolt, L. Haupt, K. Bärner, and U. Sondermann, "Metal-semiconductor-transition and spin-glass properties of $La_{(2-x)/3}Ba_{(1+x)/3}Mn_{1-x}Cu_xO_3$", Solid State Communications, **82**, 693-696 (1992).

[34] D. B. Chrisey and G. K. Hubler, Eds. *Pulsed Laser Deposition of Thin Films*; J. Wiley: New York, 1994.

[35] R. K. Singh, O. W. Holland and J. Narayan, "Theoretical model for deposition of superconducting thin films using pulsed laser evaporation technique", J. Appl. Phys. **68**, 233-247 (1990).

[36] T. S. Lai, W. F. Liao, H. F. Cheng and I. N. Lin, "Epitaxial growth and characteristics of the YBCO/STO/YBCO tunneling junctions", C. J. Phys. **36**, 2-11 (1998).

[37] T. Y. Yum, "The study of structural, dielectric and pyroelectric properties of SBN compositional graded film", M.Phil Thesis, The Hong Kong Polytechnic University, (2005).

[38] B. Nadgorny, I. I. Mazin, M. Osofsky, R. J. Soulen, P. Broussard, R. M. Stroud, D. J. Singh, V. G. Harris, A. Arsenov and Ya. Mukovskii, "Origin of high transport spin polarization in $La_{0.7}Sr_{0.3}MnO_3$: Direct evidence for minority spin states", Phys. Rev. B **63**, 184433 (2001).

[39] J. Dho, N. H. Hur, I. S. Kim and Y. K. Park, "Oxygen pressure and thickness dependent lattice strain in $La_{0.7}Sr_{0.3}MnO_3$ films", J. Appl. Phys. **94**, 7670-7674 (2003).

[40] J. Z. Sun, D. W. Abraham, R. A. Rao and C. B. Eom, "Thickness-dependent magnetotransport in ultrathin manganite films", Appl. Phys. Lett. **74**, 3017-3019 (1999).

[41] Y. S. Du, B. Wang, T. Li, D. B. Yu and H. Yan, "Effects of annealing procedures on the structural and magnetic properties of epitaxial $La_{0.7}Sr_{0.3}MnO_3$ films", J. Magn. Magn. Mater. **297**, 88-92 (2006).

[42] C. Y. Lam, "Semiconducting properties of oxide thin films prepared by pulsed laser deposition", M.Phil Thesis, The Hong Kong Polytechnic University, (2004).

[43] J. R. Sun, H. W. Yeung, H. K. Wong, T. Zhu, and B. G. Shen, "Effects of vacuum annealing on the transport property of La Sr MnO films", The European Physical Journal B - Condensed Matter and Complex Systems **35**, 481-491 (2003).

[44] B. S. H. Pang, C. Bell, R. I. Tomov, J. H. Durrell, and M. G. Blamire, "Pseudo spin-valve behavior in oxide ferromagnet/superconductor/ferromagnet trilayers", Phys. Lett. A **341**, 313-319 (2005).

[45] Y. Lu, X. W. Li, G. Q. Gong, G. Xiao, A. Gupta and P. Lecoeur, "Large magnetotunneling effect at low magnetic fields in micrometer-scale epitaxial $La_{0.67}Sr_{0.33}MnO_3$ tunnel junctions", Phys. Rev. B **54**, R8357-R8360 (1996).

[46] A. Ruotolo, A. Oropallo, F. Miletto Granozio, G. P. Pepe, P. Perna and U. Scotti di Uccio, "Magnetic and magnetotransport properties of $La_{0.7}Sr_{0.3}MnO_3$/Permalloy

heterostructures", Appl. Phys. Lett. **88**, 2504 (2006).

[47] M. P. Singh, B. Carvello and L. Ranno, "Giant magnetoresistance in an all-oxide spacerless junction", Appl. Phys. Lett. **89**, 022504 (2006).

[48] R. J. M. Van de Veerdonk, J. Nowak, R. Meservey, J. S. Moodera and W. J. M. de Jonge, "Current distribution effects in magnetoresistive tunnel junctions", Appl. Phys. Lett. **71**, 2839-2841 (1997).

[49] J. Zhu, L. Zheng, Y. Zhang, X. H. Wei, W. B. Luo and Y. R. Li, "Fabrication of epitaxial conductive $LaNiO_3$ films on different substrates by pulsed laser ablation", Materials Chemistry and Physics **100**, 451-456 (2006).

[50] R. P. Borges, W. Guichard, J. G. Lunney and J. M. D. Coey, "Magnetic and electric "dead" layers in $(La_{0.7}Sr_{0.3})MnO_3$ thin films", J. Appl. Phys. **89**, 3868-3873 (2001).

[51] T. Fix, C. Ulhaq-Bouillet, S. Colis, A. Dinia, G. Bertoni and J. Verbeeck, "Nanoscale analysis of interfaces in a metal/oxide/oxide trilayer obtained by pulsed laser deposition", Appl. Phys. Lett. **91**, 023106 (2007).

[52] X. W. Li, A. Gupta, G. Xiao, and G. Q. Gong, "Low-field magnetoresistive

properties of polycrystalline and epitaxial perovskite manganite films", Appl. Phys. Lett. **71**, 1124-1126 (1997).

[53] J. Bass and W. P. Pratt, "Current-perpendicular (CPP) magnetoresistance in magnetic metallic multilayers", J. Magn. Magn. Mater. **200**, 274-289 (1999).